# Distinguishing Characteristics of the Tropical Cyclone Gigantic Jet Environment®

STEVEN M. LAZARUS, A JASON CHIAPPA, HADLEY BESING, MICHAEL E. SPLITT, AND JEREMY A. RIOUSSET

<sup>a</sup> Department of Ocean Engineering and Marine Sciences, Florida Institute of Technology, Melbourne, Florida
 <sup>b</sup> School of Meteorology, University of Oklahoma, Norman, Oklahoma
 <sup>c</sup> College of Aeronautics, Florida Institute of Technology, Melbourne, Florida
 <sup>d</sup> Department of Aerospace, Physics and Space Sciences, Florida Institute of Technology, Melbourne, Florida

(Manuscript received 1 September 2020, in final form 21 May 2021)

ABSTRACT: The meteorological characteristics associated with thunderstorm-top turbulence and tropical cyclone (TC) gigantic jets (GJs) are investigated. Using reanalysis data and observations, the large-scale environment and storm-top structure of three GJ-producing TCs are compared to three non-GJ oceanic thunderstorms observed via low-light camera. Evidence of gravity wave (GW) breaking is manifest in the IR satellite images with cold ring and enhanced-V signatures prevalent in TCs Hilda and Harvey and embedded warm spots in the Dorian and null storms. Statistics from an additional six less prodigious GJ environments are also included as a baseline. Distinguishing features of the TC GJ environment include higher tropopause, colder brightness temperatures, more stable lower stratosphere/distinct tropopause, and reduced tropopause penetration. These factors support enhanced GW breaking near the cloud top (overshoot). The advantage of a higher tropopause is that both electrical conductivity and GW breaking increase with altitude and thus act in tandem to promote charge dilution by increasing the rate at which the screening layer forms as well as enhancing the storm-top mixing. The roles of the upper-level ambient flow and shear are less certain. Environments with significant upper-tropospheric shear may compensate for a lower tropopause by reducing the height of the critical layer which would also promote more intense GW breaking and turbulence near the cloud top.

KEYWORDS: Convection; Gravity waves; Turbulence; Wave breaking; Atmospheric electricity; Convective storms; Convective-scale processes; Stability; Storm environments

#### 1. Introduction

Gigantic jets (GJs) are electrical discharges that propagate upward from thunderstorms reaching altitudes between 70 and 90 km, terminating in the lower ionosphere (Pasko et al. 2002; Su et al. 2003). The thunderstorm environment associated with jets and GJs is relatively diverse—ranging from isolated deep convection to sheared tropical disturbances. Both theory and observations indicate that enhanced storm-top mixing and the associated dilution of the negative screening layer is likely a key component of GJ events (Krehbiel et al. 2008; Lazarus et al. 2015), yet the associated meteorological conditions remain unclear. For example, extreme storm-top turbulence was observed in association with four Florida GJ events in August 2013 (Lazarus et al. 2015). While these events tracked closely with the centroid of the upper-level outflow (thunderstorm overshoot region), overshooting tops (OT hereafter) are commonplace and thus do not appear to be sufficient cause for GJ occurrence. Unlike sprites, GJs are relatively rare (Chen et al. 2008) but appear to have an affinity for sheared tropical disturbances ranging from weakening hurricanes to remnant lows. This prompts the question, are there other distinguishing

Corresponding author: Steven M. Lazarus, slazarus@fit.edu

(unique), and observable, meteorological conditions and/or corresponding storm characteristics associated with jet-producing convection that can be linked to these systems?

Boggs et al. (2018) indicate that, during the intense convective pulse, storm-top divergence advects the screening charge away from the center axis of the convection and creates a temporary "hole" in the upper negative screening layer. At the same time, shear-driven turbulent eddies form within the upper-level outflow such that the mixing (dilution) of the negative screening charge with upper positive charge occurs around the periphery of the convection rather than at the center. This is supported by evidence of enhanced spectrum width along the outer edge of the spreading anvil and relatively concentrated region of exposed positive charge at storm top (see Boggs et al. 2018, Fig. 2). While relevant to the charge structure, this model largely ignores the role of the overshoot.

Atmospheric gravity waves (GWs), which can result from a variety of processes involving vertical displacement of air parcels including convection, orography, adjustment of balanced flows, and jet stream instability are also a significant source of atmospheric turbulence. Observations of turbulence induced by orographic GW breaking reveal that significant mixing can occur near the tropopause region (Whiteway et al. 2003). Cumulus convection is also an important excitation mechanism for upper-tropospheric/lower-stratospheric (hereafter UTLS) GWs. Using GPS radio occultation data, Tsuda (2014) generated a 2-yr global climatology of GW energy showing the most intense values in the lower stratosphere extending downward into the upper troposphere of the tropical

<sup>©</sup> Supplemental information related to this paper is available at the Journals Online website: https://doi.org/10.1175/JAS-D-20-0265.s1.

equatorial regions. Thunderstorm-induced turbulence, which manifests as both convective (inside) and near (outside) cloud, is generally more intense for the former. GW breaking near the storm top has been well documented as a source of severe turbulence associated with deep convection (Fovell et al. 1992; Pfister et al. 1993; Piani et al. 2000; Lane et al. 2003; Lane and Sharman 2008; Lane et al. 2012). In particular, the GW spectrum has been shown to be sensitive to upper-tropospheric wind shear (Beres et al. 2002). For example, Lane et al. (2012) indicate that a relatively small change in wind speed above deep convection, on the order of 5-10 m s<sup>-1</sup>, can induce downshear wave breaking. In their simulations of a severe aircraft-related turbulence event above a developing thunderstorm near Dickinson, North Dakota, the enhanced shear layer was quite shallow (i.e., less than a few hundred meters deep). Turbulence along the cloud and anvil edges (referred to as cloud interfacial instability) associated with enhanced shear and flow deformation can reduce the Richardson number and support Kelvin-Helmholtz billows in these regions as well (Grabowski and Clark 1991). In addition, simulations of overshooting convection indicate wavelike wake regions downwind of collapsing OTs with their exact cause unknown (Wang et al. 2010). In their earlier work, Lane et al. (2003) distinguish local (i.e., within 1 km of cloud top) turbulence from the above-cloud (stratospheric) GW breaking. The former (latter) source is attributed to a nonlinear response to tropopause penetration (GW breaking). However, they allude to a GW-induced turbulence source directly above the updraft—which is consistent with Lazarus et al. (2015) finding that the GJ source region is closely tied to the OT (Lazarus et al. 2015). In a follow-up study, Lane and Sharman (2008) used idealized mid- to upper-tropospheric shear profiles and systematic variations in static stability to evaluate the impact on wave breaking at and above storm top. One of their key findings was that intense turbulence, due to GW breaking, occurs near the cloud top rather than in the lower stratosphere for shallow/high shear layers in the upper troposphere (the enhanced shear acts to reduce the height of the critical layer, bringing it closer to the GW source, i.e., cloud top). Their modeling results also indicated that the wave breaking was more intense for higher stormtop shear and that the near-cloud turbulence is most prevalent during the early stages of a thunderstorm's lifetime.

Using dropsonde and upper-air data, Molinari et al. (2014) show that the upper troposphere of the tropical cyclone (TC) environment tends to have low static stability [i.e., bulk Richardson number (BRN) < 1] compared to tropical rawinsondes in general. However, this signal was less prevalent for depressions and tropical storms (Duran and Molinari 2016). In particular, three basic types of low BR regions emerge, including a layer within the upper portions (>12 km) of the central dense overcast, where the turbulence criteria (i.e., BRN < 0.25) were met in 10% of the dropsonde data for the weaker storm environments [ranging from tropical depression (TD) to category 2], which is still well above the frequency for the non-TC sondes. It may be that this low upper-tropospheric stability associated with the TC environment preconditions the convective atmosphere for GJ occurrence.

Past studies of satellite observed cold rings, i.e., a warm spot surrounded by colder brightness temperatures associated with intense deep convection, have linked this feature with stratification and wind shear just above the tropopause (e.g., Setvák et al. 2010). While many OTs tend to generate an ephemeral downwind embedded warm spot (EWS) or warm area (EWA), cold rings are persistent and rarer. Similar warm regions have also been associated with the cold-U/V (enhanced-V) feature identified in IR imagery (Negri 1982; Fujita 1982; McCann 1983; Heymsfield et al. 1983). Heymsfield et al. (1983) suggested that the warm spot in proximity of the OT was an artifact of the descending motion associated with a breaking GW. Cold ring and enhanced-V signatures have been directly related to the occurrence of upper-tropospheric GW breaking (Wang 2007; Luderer et al. 2007) and, more recently, to above anvil cirrus plumes (AACPs; Wang 2003, 2004; Homeyer et al. 2017; Bedka et al. 2018).

Here we present case studies of two prolific GJ producing tropical cyclones, Harvey and Hilda, and revisit the convection generated by Tropical Depression Dorian in August 2013, which produced four GJs (Lazarus et al. 2015). Using reanalysis data and observations, the ambient meteorological conditions of the UTLS, in particular the ambient flow, static stability, tropopause height and shear of GJ storm environments are compared to three non-GJ events associated with isolated oceanic thunderstorms observed via a low-light camera. A second, less prodigious, group of GJ-producing convection (two of which are tropical storms) is included in order to provide a baseline for the TC GJ storms. Both satellite IR images and radar data (when available) are used to assess storm-top characteristics and structure. The critical aspects that differentiate the ambient environments of the GJ and null storms are then discussed.

## 2. Storm summary

A brief summary of Hurricane/Tropical Storm (TS) Hilda, Tropical Storm Harvey, and the null events is presented here, while TD Dorian and associated GJs are described in Lazarus et al. (2015).

# a. Hilda

Hilda produced at least 21 GJs on consecutive evenings of 11-12 August 2015 (12 and 9 events; referred to here as Hilda1 and Hilda2, respectively, in Table 1). Event times were extracted from time-lapse video (40-s exposures) obtained from the east-facing Canada France Hawaii Telescope (CFHT) CloudCam on top of Mauna Kea. The GJ event time window was just over an hour on the first evening and 15 min on the second night. The cyclone, which was christened on 6 August, intensified rapidly on 7 August, and became a major (category 4) storm the following day (Blake and Jelsema 2016). As the system gained latitude it began to encounter increasing westerly flow (shear) associated with the subtropical jet stream near Hawaii. Rapid weakening began on 11 August and Hilda weakened to a tropical storm by 0000 UTC 12 August. Thereafter, the storm remained almost stationary, losing most of its deep convection by 13 August.

TABLE 1. Hilda event times (UTC) for 11 (Hilda1) and 12 (Hilda2) Aug 2015.

Event No.	11 Aug 2015	12 Aug 2015		
1	0618:19	1237:37		
2	0653:00	1238:57		
3	0654:20	1240:17		
4	0657:00	1240:57		
5	0657:40	1242:57		
6	0659:00	1243:37		
7	0702:20	1244:57		
8	0711:40	1244:57		
9	0715:00	1251:37		
10	0717:40			
11	0725:40			
12	0730:20			

#### b. Harvey

On the evening of 18 August 2017, a minimal Tropical Storm Harvey passed south of Puerto Rico. Between 0400 and 0900 UTC there were 18 GJs observed by an amateur photographer, Frankie Lucena, via a low-light camera [Watec 902H Ultimate camera system, 768 × 494 pixels, 12-mm F/1.2 lens, 32° horizontal field of view (FOV)] situated on the southwest coast of Puerto Rico (e.g., Fig. 1). On 17 August, Harvey strengthened to a tropical storm east of Barbados (Blake and Zelinsky 2018). While passing south of the island, Harvey encountered strong northerly shear, weakening to a depression early on 19 August and was downgraded to a tropical wave at 1800 UTC the same day. The remnants continued on a west-northwest track through the Caribbean before emerging in the southwest Gulf of Mexico on 23 August. Harvey then quickly intensified into a hurricane on 24 August, becoming a major hurricane the following day, making landfall as a category 4 storm on the Texas coast on 26 August. The locations of eleven of the GJs that were identified from the GOES-16 Geostationary Lightning Mapper (GLM) data are provided in Table 2 (Boggs et al. 2019). The GJs were identified by pairing GLD360 (Said et al. 2013) events with the time stamp and direction of the ground-based images. There were approximately three GLD360 detections per identified GJ. The GLM GJs had three distinguishing characteristics compared to other flashes including longer continuous emissions and optical energies and diminished lateral propagation (Boggs et al. 2018).

#### c. Null events

A low-light camera mounted on the Olin Physical Sciences building roof on the Florida Tech campus has been part of a transient luminous event (TLE) observing effort for the past several years (Liu et al. 2015). During the summer of 2018, 86 sprite events were observed in association with deep convection (no GJs were observed during this period). On the evenings of 8 and 25 July, there was deep convection located offshore southwest and east-central Florida, referred to as Null1 and Null2, respectively. Extended videography (see the online supplementary material) indicated frequent lightning; however, no TLEs were observed throughout the lifetime of either storm. The third storm, Null3 (23 July 2019), is associated with a brief tropical depression and associated nocturnal convective burst that developed over the northwestern Bahamas and then dissipated off the east coast of Florida the next day (Zelinsky 2019). In each case, the camera had an unobstructed view of the storm top as there were no intervening clouds (the anvil debris was blown downwind away from the camera).

#### 3. Results

The mechanisms responsible for near- and above-cloud-top turbulence can vary and include both shearing instabilities (e.g., flow deformation) and/or GW breaking. The disturbed environment is examined here using radar and satellite data while the background flow and ambient static stability are assessed using reanalysis and radiosondes. The reanalysis product is ECMWF's fifth-generation dataset (ERA5), which provides global gridded data on the order of 0.25° spatial, 1-h temporal, and variable vertical resolution (137 levels). In particular, the product has relatively high resolution in the UTLS (on the order of 300 m) which is important for tropopause height and structure (Hersbach et al. 2020).

# a. Upper-level outflow

Given Hilda's distance from Hawaii, the radar analysis presented here is limited to the three null events, Dorian, and



FIG. 1. The last two observed gigantic jets from Tropical Storm Harvey on 19 Aug 2017 (Table 2): (left) 0846:02 and (right) 0850:16 UTC. Image courtesy of amateur photographer Frankie Lucena. For a video of the Harvey events, see the online supplementary material.

TABLE 2. Harvey event times (UTC), GLM-identified locations from Boggs et al. (2019), local brightness temperature minimums (BT<sub>min</sub>), and relative location with respect to the *GOES-16* band 13 IR features. For radar purposes, HA1 and HA2 are used to distinguish the rainband GJ events (see Table 8).

Event No.	Time	Lat (°N)	Lon (°W)	$BT_{min}(K)$	Region
1	0419:54	13.28	65.77	182.6	Central canopy
2	0421:15	13.20	65.85	182.6	Central canopy
3	0424:46	13.27	65.84	182.6	Central canopy
4	0427:33				• •
5	0539:05				
6	0612:39	13.36	65.67	183.8	East canopy
7	0639:01	13.80	66.73	185.5	Central canopy
8	0701:53	14.58	66.39	183.8	North canopy
9	0709:59				
10	0718:33	13.59	65.88	186.3	East canopy
11	0725:41	16.01	65.21	195.8	Rainband (HA1)
12	0728:51				,
13	0755:17				
14	0814:38	14.66	66.46	186.8	East canopy
15	0819:52				17
16	0828:27				
17	0846:03	15.90	67.09	193.8	Rainband (HA2)
18	0850:16	15.90	67.09	193.8	Rainband (HA2)

Harvey (on the second evening, Hilda is just close enough, 450 km, to the Honolulu, Hawaii, radar PHWA to obtain a rough estimate of storm top only). Figure 2 shows radar data for the storm that produced the last two Harvey GJs (17 and 18, Table 2), which occurred along a rainband approximately 200 km south of the San Juan radar (TJUA). The earlier rainband storm that produced GJ 11 was range folded and thus radial velocity data are not available. The Null1 and Null2 storms are sampled from the Key West (KBYX) and Jacksonville (KJAX) radars, respectively, while both the Melbourne (KMLB) and Miami (KAMX) radars are used for Null3. Base (PPI) reflectivity and the corresponding vertical (RHI) cross sections of reflectivity and radial velocity (along the dotted lines) are provided. When possible (in the absence of aliasing), the maximum tilt scan times were selected near peak storm intensity which, for Harvey, was approximately 1 min after the 0846:03 UTC GJ. In terms of maximum reflectivity and vertical extent, the most intense convection is associated with the Null1 storm off the southwest Florida coast. A characteristic upper-level divergence signature is present in each of the cross sections. Estimates of the maximum outbound and inbound radial wind speeds were obtained from the radar tilts that intersect the storm top (these are not necessarily from the same azimuth). Results are shown for the three null storms, the rainband storm that produced the last two Harvey GJs and, for comparison, TD Dorian (Table 3). Dorian and Null1 have comparable differences between the maximum inbound/outbound radial velocities ( $\Delta v_r$ , 60 vs 57 m s<sup>-1</sup>, respectively) while the Harvey storm is much lower (27.5 m s<sup>-1</sup>). The scan time, beam height/tilt, and distance from radar apply to the radial outflow (divergence) estimate only. The divergence, which is calculated along the same radial and tilt, is largest for the null storms. While studies of intense deep convection have shown that the upperlevel divergence tends, on average, to be larger for severe storms (e.g., Bedka et al. 2018), it is a common attribute of thunderstorms. Although the null storms and Harvey GJ cell are located at a comparable distance from their respective radars, given the ephemeral nature of pulse convection and rapid evolution of the rainband, it is possible that the peak upper-level outflow for the Harvey GJ cell was not captured (however, the others could also be higher). Regardless, the Null1 storm-top divergence is similar to that of the well-observed TD Dorian which produced four GJs (Lazarus et al. 2015)—about half that of Null2. All values reported here are well below the peak reported for a giant hail producing Oklahoma supercell storm which were in excess of 150 m s<sup>-1</sup> (Witt et al. 2018). While this does not eliminate the possibility that the upper-level storm outflow plays a role, it does not appear to be exceptional in the GJ storms.

#### b. Satellite features

Although gravity wave generation and breaking cannot be directly evaluated without model simulations, it can be inferred through the satellite related features. IR images are presented for both the TC GJ and null storms.

## 1) HURRICANE HILDA (11 AUGUST 2015): HILDA1

A time series of *GOES-15* band 4 minimum brightness temperatures (BT) and Hilda GJ event times (Table 1) during the first of two evenings is shown in Fig. 3. Based on the routine schedule (https://www.ospo.noaa.gov/Operations/GOES/15/imager-routine.html), footprint location and scan strategy, the time stamp shown (i.e., when the image was created) is ~10 min after the storm was sampled by the satellite. The missing BT at 0615 UTC is a result of satellite data processing. Because the tropopause environment varies across these cases, the difference between the minimum BT versus the observed and ERA5 tropopause temperatures is shown in Table 4. Given that differences are relatively large and negative (-8.1°C

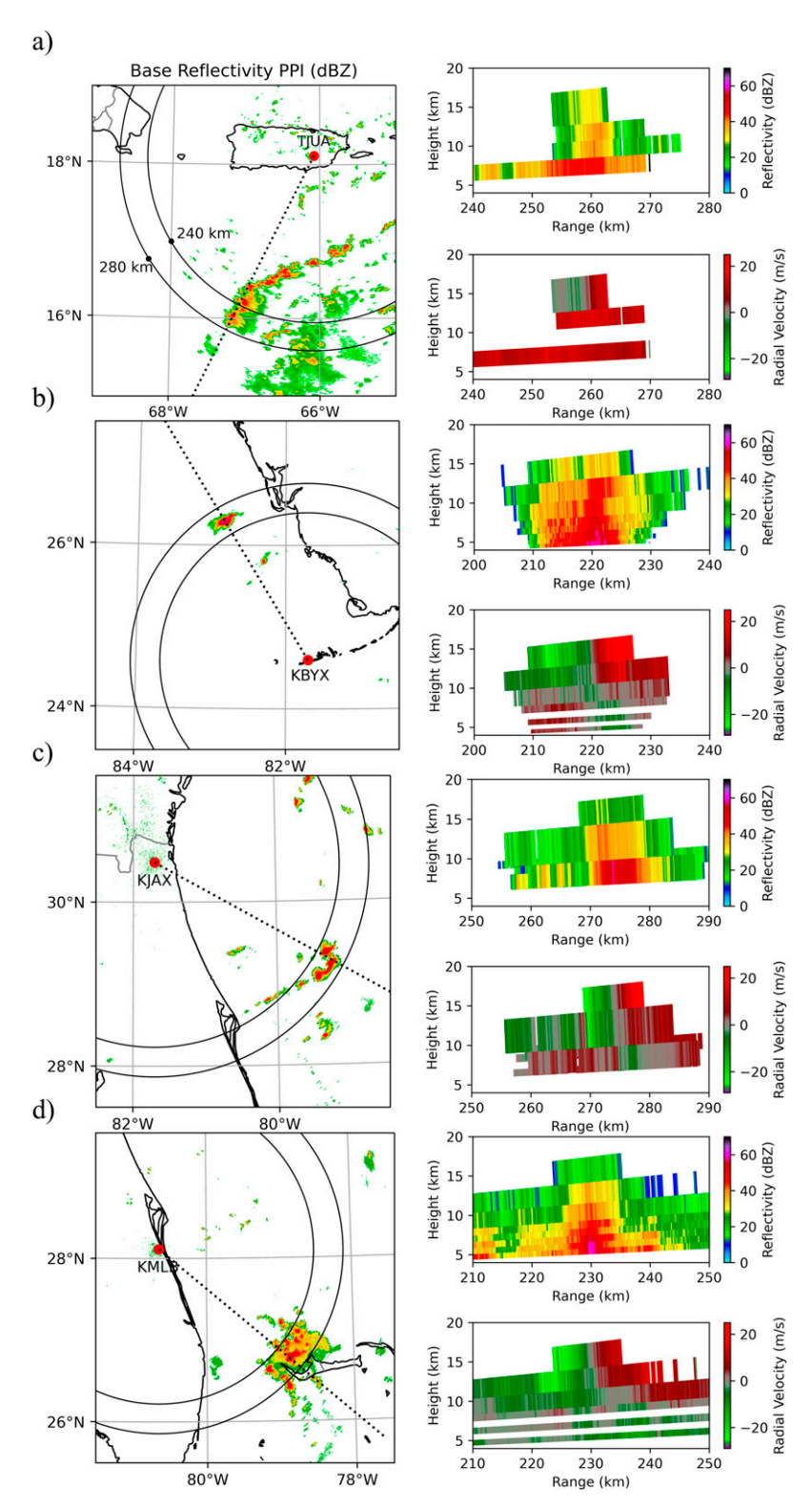


FIG. 2. (left) Base reflectivity PPI and (right) reflectivity RHI and radial velocity near peak intensity for the (a) TJUA radar at 0845 UTC 19 Aug 2017 for Harvey (GJs 17/18, see Table 1); (b) KBYX radar at 0448 UTC 9 Jul 2018 for Null1; (c) KJAX at 0434 UTC 26 Jul 2018 for Null2; and (d) KMLB at 0501 UTC 23 Jul 2019 for Null3. The dotted line in each PPI shows the RHI radial and the two range rings indicate the start and end range of the respective RHI. Image generated using Py-ART (Helmus and Collis 2016).

TABLE 3. Storm-top radar statistics from TJUA, KMLB, KBYX, KJAX, and KMLB for GJ storms from Harvey and Dorian, Null1, Null2, and Null3, respectively, along with maximum inbound and outbound radial velocities (and the difference  $\Delta v_r$ ). The outbound velocity is sampled within a  $\pm 45^\circ$  azimuthal angle with respect to the maximum inbound radial for the same tilt and time. The maximum  $v_r$  divergence is estimated by dividing the difference in the radial velocity by the distance along a single radial. The distance from the radar and beam height represent the centroid of the divergence estimate at the scan time of the storm-top tilt.

Event	Scan time	Tilt (°)	Range (km)	Beam height (km)	Max inbound $(m s^{-1})$	Max outbound $(m s^{-1})$	$ ext{Max} \ \Delta v_r \ ( ext{m s}^{-1})$	$\operatorname{Max} v_r$ divergence (s <sup>-1</sup> )
Harvey	0842 UTC 19 Aug 2017	2.4	257	14.9	7.5	20.0	27.5	0.004 60
Dorian	0359 UTC 3 Aug 2013	10	81	14.8	39.5	20.5	60.0	0.005 84
Null1	0447 UTC 9 Jul 2018	3	217	14.3	25.0	32.0	57.0	0.005 79
Null2	0449 UTC 26 Jul 2018	2.4	277	16.2	25.0	24.0	49.0	0.009 13
Null3	0502 UTC 23 Jul 2019	3.1	230	15.7	25.5	15.5	41.0	0.004 00

for both the ERA5 and sounding) and that the observed cold point and tropopause temperatures are the same (Table 7), indicates the OT is well above the tropopause. The initial GJ is somewhat isolated in that it occurs 35 min prior to the event cluster and occurs (~15 min) before the time of the coldest cloud tops while the remaining GJs occur as the minimum cloud-top temperature warms (by  $\sim 3$  K). Half (six) of the events occur within a 9-min window following the time (0645 UTC) of the minimum GOES-15 BT (187 K, Table 4). After an approximate 9-min interlude, three additional GJs occur over a 6-min period followed by a second lull on the order of 8 min and then the final two events, which occur approximately 5 min apart. A succession of 12 IR satellite images ranging from 0530 to 0845 UTC (15 min between scans) are shown in Fig. 4 (for an animation, see the online supplementary material). The panels show the evolution of a cold-U/V feature at various stages—beginning with a narrow elongated "close-in" warm area (CWA; Heymsfield et al. 1983) and associated cold U shape that eventually broadens into more of a V shape (Setvák et al. 2010). The persistence of the enhanced V places the event on the high side with respect to longevity (Setvák and Rabin 2003). The coldest BTs, which are embedded in the eastern arm of the U/V, undergo subtle changes during the 3-h window but their location is for the most part stationary with respect to the feature. Hilda's circulation center is southeast of the CWA throughout the event window, in the right-front storm quadrant, which tends to be a region of enhanced storm-relative helicity (SRH)—even for overwater storms (Sueki and Niino 2016). The bulk 1-km tropopause shear vector (gray arrow in the first panel in Fig. 4 and Table 5), selected from the maximum of the ERA5 profiles within 2 km of the tropopause, points to the west while the deep-layer shear vector (i.e., 850–200 hPa, black arrow), an average of the ERA5 profiles, is directed opposite (southeast).

### 2) TROPICAL STORM HILDA (12 AUGUST 2015): HILDA2

The deep convection associated with the second evening of GJ events is quite different. A total of nine events were observed within a 14-min interval and, with the exception of the last GJ, the time between events were comparatively short (less than 1 min apart) with respect to the previous day. The associated minimum BT time series indicates a steady decrease

of 11 K between 1100 and 1230 UTC and a minimum around 189 K (Fig. 5, Table 4). Taking into account the time stamp discrepancy, the GJ event cluster occurs about 20 min after the first BT minimum—during a window in which the minimum cloud-top temperatures warm (by ~3 K). The difference between the minimum BT and observed (ERA5) tropopause temperatures are  $-5.8^{\circ}$ C ( $-7.2^{\circ}$ C), respectively, which are less than that of Hilda1. Similar to Hilda1, the slight difference between observed cold-point and tropopause temperatures (0.2 K, Table 7) supports an OT that is well above the tropopause. The corresponding GOES-15 band 4 BTs, from 1100 to 1415 UTC, are shown in Fig. 6 (for an animation, see supplementary material). The absence of visible satellite data (and radar) makes it difficult to unambiguously associate regions of cold pixels with OTs as these features might be related to other cloud-top signatures. Hence, in the absence of supporting radar data or other obvious storm structure such as a downwind detraining anvil, cold IR pixels are referred to here to as cold cloud tops (CCTs). There are two distinct areas of CCTs in the 1130-1145 and 1145-1200 UTC images. In the 1230-1245 and 1245-1300 UTC images, a clearly defined cold ring with a central warm spot (CWS; Setvák et al. 2010) can be seen while the coldest BTs have diminished to just a few pixels embedded along the southern edge of the CWS (1230–1245 UTC) and the ring perimeter (1245-1300 UTC). All nine GJ events occur within the timeframe of these two panels (delineated by a gray border). By 1300–1315 UTC, the northeast portion of the ring begins to erode (warm). As in the previous evening, the deep convection occurs north of the storm track with the circulation center near the southern portion of the cold ring during the GJ time window (1230-1300 UTC). The slow southwestward storm motion places the convection in the right-rear quadrant while the deep-layer and tropopause shear are in the same directions (northwesterly, first panel Fig. 6). Although the cold ring itself warms over the latter portion of the window, the minimum BT decreases (from 1315 to 1400 UTC) in response to a small region of CCTs that are evident in the last three images. This second BT minimum is slightly cooler (by about 1°C) than the earlier one at 1230 UTC; however, there were no observed GJs after 1251:37 UTC (Table 2) and the convection subsequently decays with BTs warming from 188 to 195 K between 1415 and 1500 UTC (not shown).

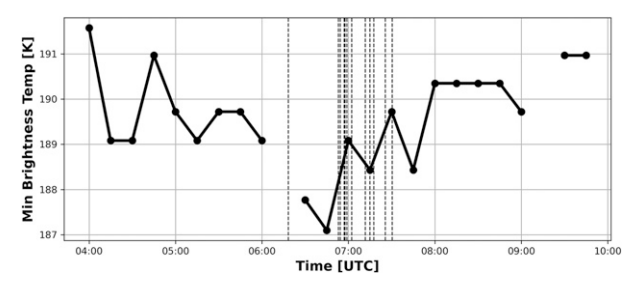


FIG. 3. Time series of *GOES-15* band 4 minimum brightness temperatures (K) for Hilda night 1 (11 Aug 2015, Fig. 4). The GJ event times are indicated by dashed vertical lines.

#### 3) TROPICAL STORM HARVEY (18 AUGUST 2017)

Time series of minimum BT and the accompanying GOES-16 band 13 IR images are shown in Figs. 7 and 8, respectively (for an animation, see the supplementary material). Because the Harvey GJ events span a 5-h window, the IR images are not continuous. Also, due to the large spatial extent of the convection, two separate regions are used to distinguish between the central and rainband convection, Harvey1 and Harvey2, respectively (details are provided in section 3c). The 12 GJ events identified in Boggs et al. (2019) are depicted as cyan rings in the panels with gray borders. While Hilda's GJs occur in conjunction with a relatively large scale and well-defined enhanced-V and cold-ring signatures, several of the Harvey GJs appear to be associated with small-scale and short-lived convective bursts and EWSs and/or CWSs located in specific regions of the weakening tropical cyclone. As there are no definitive BT characteristics nor spatiotemporal scales that separate an EWS and CWS, the two are used interchangeably here [although Setvák et al. (2010) classify the EWS as the more transient of the two features]. While a "warm trench" adjacent to the OT region is a common feature in deep convective storms, a temporally persistent and spatially spreading warm area is suggestive of GW breaking and perhaps cirrus spreading downwind.

Although there appears to be some ringlike structure in the early images, well-formed (distinct) cold rings are not readily apparent until the later GJ events (i.e., after 0745 UTC). Four of the 18 events occur just prior to the coldest BT (178 K) at 0445 UTC (Fig. 7) while the remaining events are distributed over a 4-h period where the minimum BTs fluctuate but

gradually warm by about 10 K. The BT-tropopause temperature differences in the Harvey1 region are the largest of the environments presented  $(-13.1^{\circ}\text{C})$  for both the observed and ERA5). Given the slight difference between the observed cold point and tropopause temperatures (0.2 K, Table 7), this supports penetrative OTs that extend well above the tropopause. The first three GJ events (0415-0426 UTC, Fig. 8) occur in a cluster along or near the eastern edge of a cold ring and CWS located just south of the NHC best track circulation center (~13.4°N, 66.3°W). At this time, the ring radius is ~30 km—about half that of the Hilda2 feature. The ringlike structure begins to fragment along its northern perimeter—presenting as more of a disorganized enhanced V with a north-south-oriented CWA (0430-0441 UTC). At 0545-0556 UTC, a larger (~50 km radius) partial ring is evident with the coldest BTs south and west of a CWS located along the storm track (to the west of the circulation center). The CWS (~13.7°N, 66.3°W) persists over three consecutive scans and is also small compared to that of Hilda2 (10 vs 30 km across, respectively). Other subtle but interesting features can also be seen in this image such as a small crescent-shaped sliver of CCTs to the east of the ring (~13.5°N, 66.5°W). An even smaller area of CCTs in the northern portion of the cirrus anvil (~14.5°N, 66.4°W) propagates southward relative to the canopy and develops a crescent-like shape from 0600-0611 to 0615-0626 UTC. This location (i.e., where the north edge of the large cirrus canopy and rainband convection intersect), is convectively active and is a source region for several of the later GJs (i.e., 0700-0711 UTC and 0815-0826 UTC). The eastern portion of the main convective region (along and just north of the storm track, ~13.5°N, 65.8°-66.0°W) is also active, producing two of the GLM-identified GJs (at 0600–0611 and 0715–0726 UTC), and a distinct cold ring in three successive IR panels between 0745 and 0826 UTC. The cold ring expands from a radius of about 25 to 50 km and tracks closely with the circulation center (the location that corresponds to the image time is delineated by a circle with an embedded cross). During this time frame, the camera captured two GJ events (at 0819:52 and 0828:27 UTC, Table 2) but their GLM locations were not identified. In the following two IR panels (0830-0841 and 0845-0856 UTC) the cold ring warms and takes on the appearance of an enhanced V as the CWS transforms into an east-west-oriented CWA.

Three of the GJs occur along two short-lived rainbands that develop and extend to the northeast of the main convective

TABLE 4. The event, minimum GOES IR channel brightness temperatures ( $BT_{min}$ ), and the difference from the observed and ERA5 WMO tropopause temperatures (trop temp). Also shown are the GOES platform and IR band number.

Event	$BT_{min}(K)$	$BT_{min}$ – observed trop temp (K)	$BT_{min} - ERA5 \text{ trop temp } (K)$	GOES	Band No.
Null1	202.0	-1.8	-2.8	16	13
Null2	198.3	-7.9	-6.0	16	13
Null3	200.1	-4.3	-3.0	16	13
Hilda1	187.1	-8.1	-8.1	15	4
Hilda2	188.4	-5.8	-7.2	15	4
Harvey1	179.5	-13.1	-13.1	16	13
Harvey2	191.8	-4.8	-0.7	16	13
Dorian	197.7	-0.9	-5.6	13	4

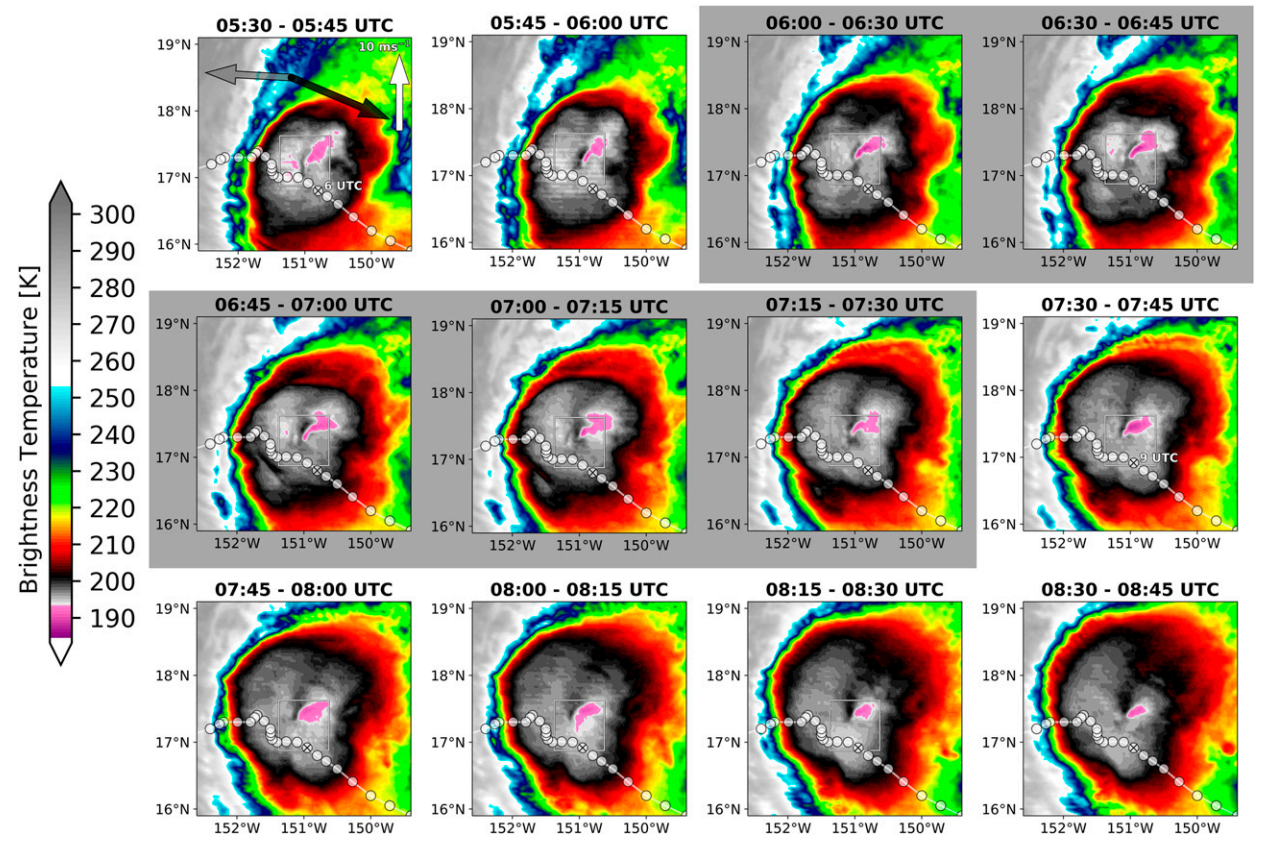


FIG. 4. GOES-15 band 4 brightness temperatures (K) for Hilda night 1 (11 Aug 2015). Scans that include GJ events are highlighted with a gray border. Also shown is the storm track from the IBTrACS database (Knapp et al. 2010, 2018) and ERA5 footprint for the times that were sampled (thin white box, see text and online supplementary material for details). The TC location closest in time to the respective image is depicted by the circle with an embedded cross. The arrows shown in the first panel are the 1-km bulk shear vector (gray), obtained by selecting the maximum magnitude from the individual ERA5 profiles within ±2 km of the tropopause, and the average 850–200-hPa bulk shear vector (black). The vector scale is shown in the upper-right portion of the panel (white arrow).

region (Harvey2), one during 0715-0726 UTC and two within 0845–0856 UTC). The events are similar in that each of them occurs in close proximity to an OT located along the west edge of an eastward detraining storm anvil. An EWS can be seen with the northeast-most rainband cell (~16.1°N, 65.2°W) in the IR panel that follows GJ 10 (i.e., 0730-0741 UTC). The last two GJs (17 and 18, Table 2) are the evening's most visible (they are closest to the camera location in SW Puerto Rico, Fig. 1), occurring within a brief convective pulse along a second rainband that develops south of the San Juan radar (Fig. 2a). The two events, whose GLM locations are indistinguishable, occur 4 min apart. The local BTs in the vicinity of the last two GJs are the warmest (~194 K) of the Harvey events. The BTtropopause temperature differences in the Harvey2 region are comparatively small with respect to the ERA5  $(-0.7^{\circ}\text{C})$ although the observed difference is larger (-4.8°C). In addition, a northwest-southeast-oriented embedded warm area (~16.0°N, 67°W) can be seen in association with the rainband cell responsible for the GJs (0900-0911 UTC). A majority of the GJs occur in the right-front quadrant with respect to the westerly storm motion with the exception of the first three, which straddle the front quadrants and two that occur near the circulation center. The near tropopause maximum and bulk shear vectors for the Harvey1 and Harvey2 regions are embedded in the first and last panels, respectively. The tropopause shear, which is southeasterly (northeasterly) for Harvey1 and (Harvey2), is the largest of the GJ and null environments (Table 5). The deep-layer shear vector is northeasterly (northwesterly) for the two regions, respectively, and the magnitude is less than the tropopause shear.

## 4) Tropical Depression Dorian (3 August 2013)

For comparison purposes, satellite images and a minimum BT time series are also provided for Dorian, which produced four GJs, two blue jets, and a starter off the east-central Florida coast on 3 August 2013 (Lazarus et al. 2015). The first three GJs span a 4-min window from 0354 to 0358 UTC, while the fourth occurs roughly 13 min later (0411:38 UTC, Fig. 9). Compared to Hilda and Harvey, Dorian's cloud-top temperatures are considerably warmer with a minimum BT near the time of the events of 201 K (there were colder BTs later that evening but no other GJs were observed). The observed BT-tropopause temperature difference is the smallest of the environments presented (-0.9°C) while the ERA5 is larger (-5.6°C) but still

TABLE 5. Kinematic quantities sampled from ERA5 vertical profiles for all events including maximum 0–3-km storm-relative helicity (SRH), maximum bulk (1-km) shear vector magnitude (MAG) and (from) direction (DIR) within  $\pm 2$  km of the tropopause, and the corresponding tropopause-relative height.

Event	Max 0–3-km SRH (m <sup>2</sup> s <sup>-2</sup> )	Max 1-km shear MAG within ±2 km of tropopause (m s <sup>-1</sup> )	Max shear DIR (°)	Max shear tropopause- relative height (km)
Null1	22	16.0	316	-0.39
Null2	49	11.7	55	-0.09
Null3	46	8.6	72	0.50
Hilda1	93	13.4	102	1.39
Hilda2	133	11.1	280	0.50
Harvey1	112	15.3	146	0.79
Harvey2	165	18.1	53	-0.08
Dorian	155	11.5	57	-0.99
AUG06 2019	47	12.8	117	-0.99
SEP16_2019	12	8.8	158	0.50
SEP24 2019	46	13.5	175	0.50
OCT16_2019	82	9.8	164	0.79
AUG22_2020	68	13.6	101	0.50
SEP05_2020	26	7.9	101	0.80

less than that of Null2. This discrepancy is within the uncertainty given the relatively large spread in the tropopause heights in the ERA5 sampling ( $\sigma = \pm 700 \,\mathrm{m}$ , Table 6). The proximity of the convection to the coastline, the sounding location (XMR) and satellite presentation suggest that convection associated with Dorian is less intense compared to Hilda and Harvey and more similar to that of the nulls. Prior to the GJ event times (0345– 0411 UTC), an OT appears near the northwest edge of the deep convection (0330-0345 UTC, Fig. 10). By 0345-0400 UTC (three of the GJs occur during this time window), a more pronounced OT is evident along with an area of crescent-shaped CCTs located to its southeast (for an animation see supplementary material). During the fourth and final GJ (0400–0415 UTC) there is an EWS; however, the OT associated with the northwesternmost cell is no longer apparent. For the remaining hour shown (0430-0530 UTC), the EWS transforms into a more of an EWA as the CCTs preferentially increase along the northwest edge of the convection ( $\sim$ 28°N, 80°W). During this period, the cirrus anvil has advected westward toward the coast which may have obscured the observation of any additional GJs (the minimum BTs are warming at this time, however). The convection is south of the circulation center throughout the event window. This places the GJ events in the left-rear quadrant relative to storm motion and near the transition between the left-front and left-rear quadrants with respect to the southeasterly deep-layer shear vector (first panel, Fig. 10). The near tropopause maximum shear vector is northeasterly and the magnitude is comparable to Hilda2.

# 5) FLORIDA NULL EVENTS (9 AND 26 JULY 2018 AND 23 JULY 2019)

As previously discussed, the null storms produced frequent lightning, yet no GJs were observed by the low-light camera, which had an unobstructed view of the storm tops. In Fig. 11, we show only two images for each of the null cases. The Null1 storm developed off the SW Florida coast around 0345 UTC (9 July 2018) and reached peak intensity with a minimum BT (202 K) between 0430 and 0500 UTC (Figs. 11a and 12a, for

an animation see supplementary material). An EWS forms downwind (to the west) of an OT located in the eastern portion of the cirrus canopy (0447-0450 UTC). Shortly thereafter (0507-0510 UTC), the CCTs are displaced eastward and the EWS is more evident. The upper-level easterly flow is quite strong (comparable to that of the Harvey1 region, not shown) and the northwesterly tropopause shear vector is large (16 m s<sup>-1</sup>, Fig. 11 and Table 5)—second only to Harvey2, while the deep-layer shear is easterly and its magnitude is the largest of the nulls and comparable to that of Hilda1. The Null2 convection is comprised of 2 multicellular storm clusters off of the east-central Florida coast that form around 0400 UTC (26 July 2018, Fig. 11b). The northern cell reaches maximum intensity between 0445 and 0515 UTC while the southern cell peaks later around 0545 UTC (see supplementary animation). The coldest brightness temperatures (198 K, Fig. 12b) occur in association with the northern cell, around 0448 UTC. OTs are present in both storms (0543 UTC) as is downwind (northeast) anvil warming (i.e., the notch of warmer BTs). Based on the 0000 UTC JAX sounding, both the upper-tropospheric and lower-stratospheric flow are southwesterly (though much weaker for the latter), while the ERA5 indicates

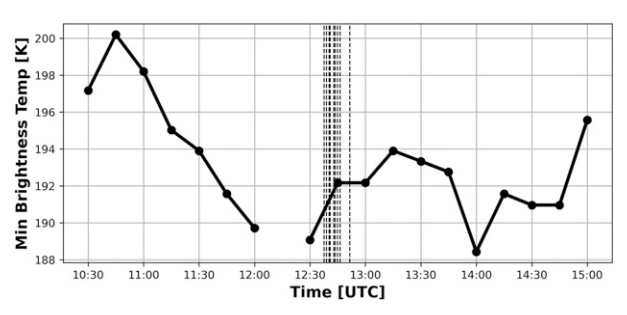


FIG. 5. As in Fig. 3, but for Hilda night 2 (12 Aug 2015, for corresponding image see Fig. 6).

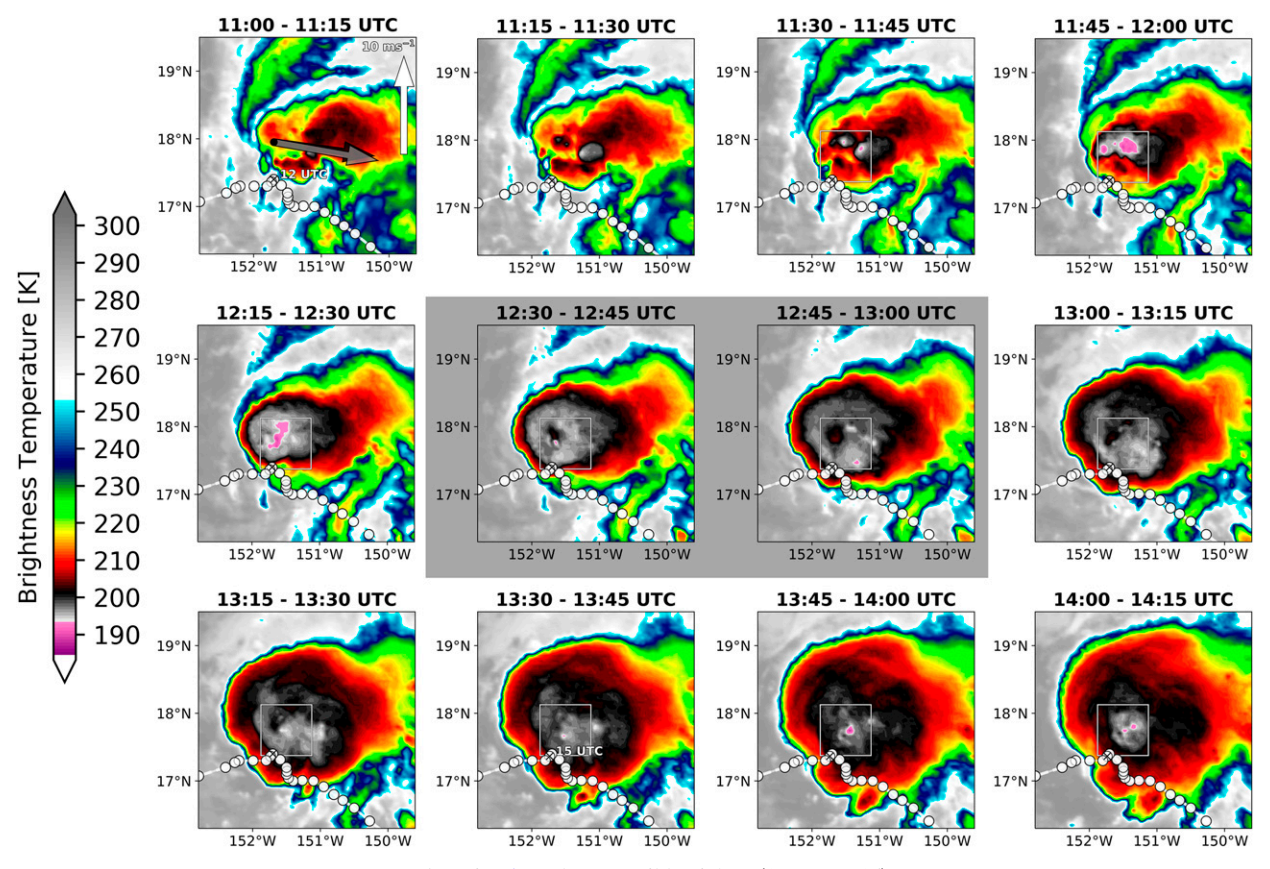


FIG. 6. As in Fig. 4, but for Hilda night 2 (12 Aug 2015).

northeasterly (southwesterly) tropopause (deep layer) shear, respectively. Null3 is associated with several distinct nocturnal convective bursts, the first of which begins around 0200 UTC 23 July 2019 just to the east of West Palm Beach, Florida (for an animation see supplementary material). A second, more substantial burst, begins around 0400 UTC north of Grand Bahama and persists through 0600 UTC before becoming stratiform and producing three visible sprites (see supplemental animation). The bursts are manifest in the BT time series with minimums at 0215 and 0500 UTC (Fig. 12c). A third burst develops approximately 100 km east of the KMLB radar at approximately 1000 UTC and continues after sunrise. Although the latter convection produces the coldest BTs, the anvil obscures the cloud tops after about 0800 UTC. The observed BT-tropopause temperature differences for Null1 and Null3 are relatively small and less than the Hilda and Harvey environments (Table 4). Null2 has larger differences (for both observed and ERA5) that are comparable to that of Hilda and the Harvey1 region. The tropopause and deep-layer shear vectors are unremarkable (the smallest magnitude of the nulls) and are northeasterly (northwesterly), respectively (Table 5).

# c. UTLS ambient flow

Without explicit model simulations, it is not possible to ascertain the characteristics of the storm impacted environment; however, the presence of cold ring and enhanced-V features in the IR imagery support the presence of gravity waves and GW breaking. It has been shown that strong flow in the UTLS can impact gravity wave dynamics at storm top (e.g., Lindsey and Bunkers 2005). In their discussion of stratospheric moisture injection associated with AACPs, Homeyer et al. (2017) indicate that a combination of deep penetrative convection and strong flow in the UTLS is

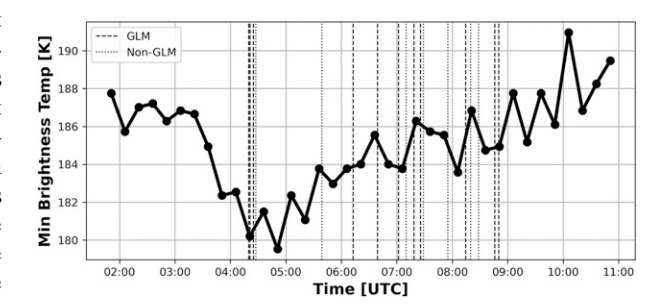


FIG. 7. As in Fig. 3, but for *GOES-16* band 13 minimum brightness temperature for TS Harvey (19 Aug 2017; for corresponding image, see Fig. 8). GJ event times identified from the GLM are indicated by dashed vertical lines and the remaining GJ event times (unidentified by GLM but present in the video, see the online supplementary material) are indicated by dotted vertical lines.

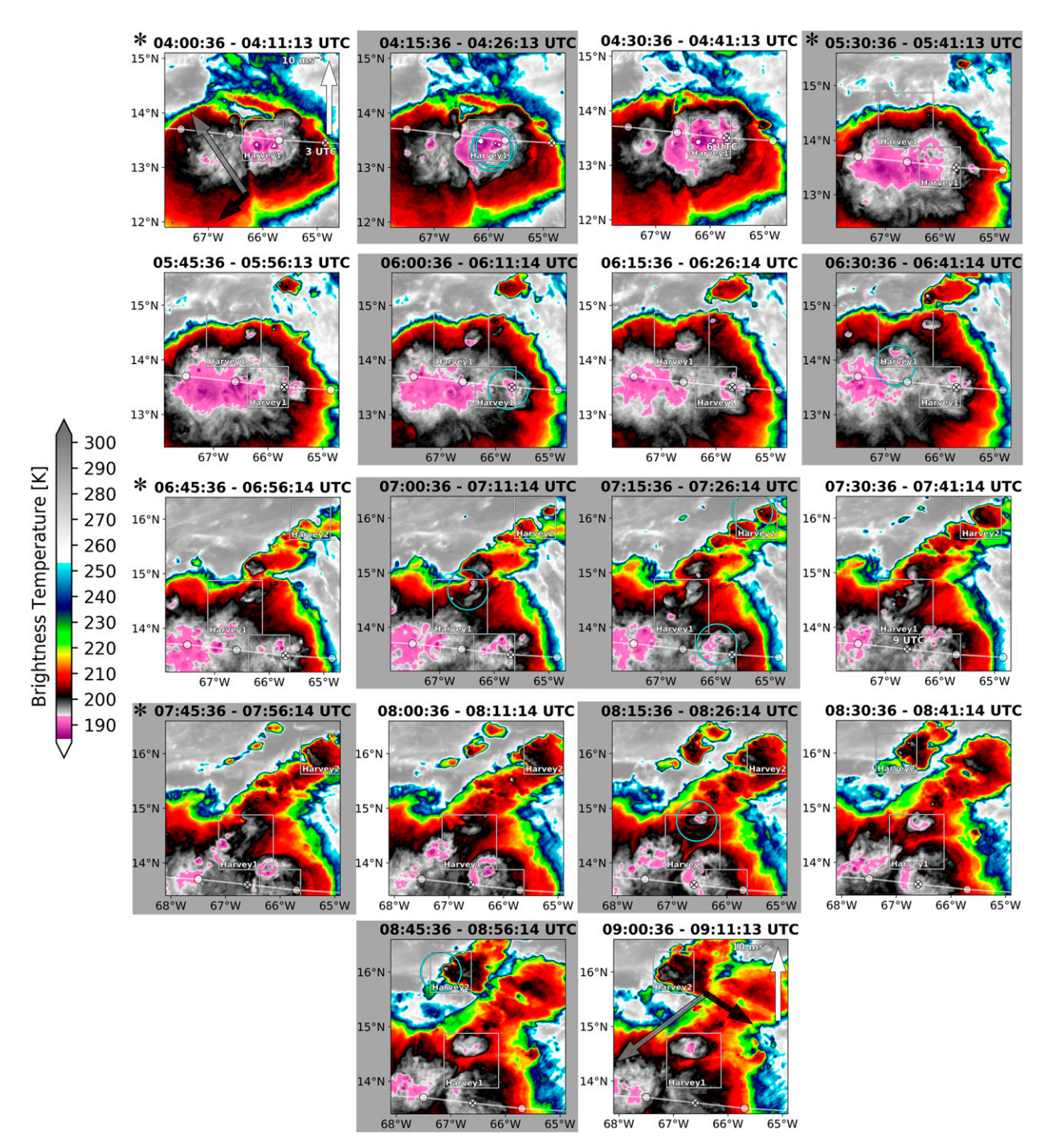


FIG. 8. As in Fig. 4, but for *GOES-16* band 13 brightness temperature (K) for TS Harvey (19 Aug 2017). The GJ locations, which are based on (corrected) GLM data (Boggs et al. 2019), are plotted as cyan rings. The footprints (boxed regions labeled Harvey1 and Harvey2) are adjusted over the event window with the first shift at 0530 UTC, a second at 0645 UTC, and final one at 0745 UTC (the shift times are delineated by an asterisk on the time stamp). The panels are contiguous in time (every 15 min) except for the 1-h jump between 0430 and 0530 UTC when there were no observed GJs. The shear vectors in the first and last panel are for the Harvey1 and Harvey2 regions, respectively.

necessary for frequent GW breaking near the OT. Dauhut et al. (2018) show that the intense mixing inside the OT is related to both wind shear and GW breaking. The shear is attributed to the large horizontal velocities associated with

the storm-induced upper-level divergence (flow deformation) while the GW generation and breaking by the OT is a result of the buoyant parcels oscillating about their level of neutral buoyancy. Furthermore, GWs that propagate in the

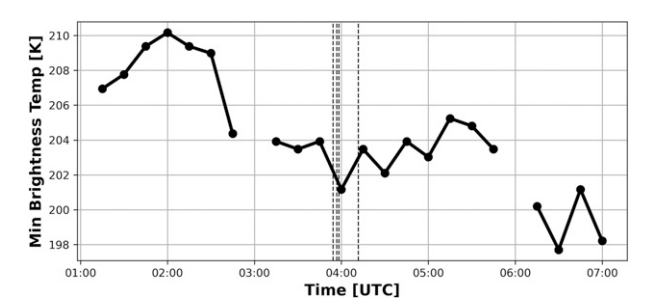


FIG. 9. As in Fig. 3, but for TD Dorian (3 Aug 2013, for corresponding image see Fig. 10).

downshear direction at storm top are more likely to break (Lane et al. 2003). The UTLS flow is examined here by comparing the null and GJ environments. Profiles were extracted over ERA5 footprints ranging from 0.25° to 0.75° latitude–longitude boxes and time windows of 1–3 h (for details, see supplementary material). The total number of profiles sampled, in each region/subregion, varies from 18 (Dorian and Null1) to 109 (Harvey1) depending on the size of the region and length of the temporal window. Tropopause heights were estimated using the WMO definition (WMO 1957).

The corresponding UTLS ambient mean wind profiles are shown in Fig. 13b in a tropopause-relative reference frame. Null1 stands out with significant ambient flow (>25 m s<sup>-1</sup>) below the tropopause but decreases (to <10 m s<sup>-1</sup>) in the stratosphere. The Harvey regions have the largest lower-stratospheric wind speeds ranging from 15 to  $20 \, \mathrm{m \, s^{-1}}$ . The lower-stratospheric flow for Hilda1 and Hilda2, the latter of which are  $5 \, \mathrm{m \, s^{-1}}$  lower on average, may be responsible for the different features present on the two evenings (enhanced V vs

cold ring, respectively; Setvák et al. 2010). Harvey2 has a pronounced shear layer that extends across the tropopause where the winds increase from 5 m s<sup>-1</sup> to more than 15 m s<sup>-1</sup>. Dorian has a wind speed maximum at the tropopause, but it appears to be poorly resolved as it is much less pronounced than observed in the proximity sounding (see Fig. 14b). While in these cases the tropopause flow does not appear to be particularly relevant, the UTLS flow is revisited in section 4.

#### d. UTLS lapse rates

The change in static stability across the tropopause may also be important. For example, model simulations have shown that an abrupt change in the Brunt-Väisälä frequency in the vicinity of the tropopause can increase the amplitude of upwardpropagating GWs promoting both wave breaking and stronger turbulence (Gavrilov and Fukao 2004). Lane and Sharman (2008) indicate that the above-cloud turbulence increases as the stability above cloud top decreases. However, their statement applies less so to the near-cloud turbulence (within 500 m of cloud top) where there were only small changes in the simulations in which the stratospheric static stability was varied (Lane and Sharman 2008, Fig. 10). Here, the static stability of the UTLS ( $\pm 4 \text{ km}$  of the tropopause) is evaluated using the Brunt-Väisälä frequency squared  $(N^2)$  and mean UTLS temperature profiles obtained from the ERA5 (Fig. 13c). The profiles were composited using the sampling method described in the previous section.  $N^2$  is displayed relative to the mean tropopause height while the mean tropopause levels, which range from about 14.4 km (Null2) to 16.1 km (Hilda1), appear explicitly along with the corresponding temperature soundings (Fig. 13a). The Null storms have reduced static stability in the lower stratosphere with values ranging from 4 to  $6 \times 10^{-4} \,\mathrm{s}^{-2}$  compared with a range from 6 to  $8 \times 10^{-4} \,\mathrm{s}^{-2}$  in the GJ TC environments. Null3 is

TABLE 6. Thermodynamic quantities sampled from ERA5 vertical profiles including mean tropopause (trop) height, standard deviation (std dev), and temperature (temp); most unstable (MU) CAPE and equilibrium level (EL); lower-stratospheric lapse rates ( $\Gamma$ , tropopause to 4 km above); and the lapse-rate difference ( $\Delta\Gamma$ ) estimated for the layer  $\pm 4$  km of the tropopause (using the mean temperature profiles, see Fig. 14a). All maximum and mean values were obtained from the spatiotemporal footprints for each case (see text for details).

Event	Mean trop height (km)	Trop height std dev (km)	Mean trop temp (K)	Mean MU EL (km)	Mean MUCAPE (J kg <sup>-1</sup> )	Trop + 4 km $\Gamma(\text{K km}^{-1})$	$\Delta\Gamma$ $(K km^{-1})$
Null1	14.4	0.1	204.8	13.9	2353	0.03	7.14
Null2	14.6	0.1	204.3	14.3	1993	-0.52	8.30
Null3	15.8	0.3	203.1	13.5	1833	-1.00	6.17
Hilda1	16.1	0.3	195.2	15.3	1917	-3.77	11.07
Hilda2	15.7	0.2	195.6	15.0	1520	-3.47	11.59
Harvey1	15.7	0.2	192.6	15.1	1122	-3.72	12.27
Harvey2	16.0	0.2	192.5	15.4	1790	-3.39	11.20
Dorian	15.3	0.7	203.3	13.9	1716	-1.18	7.34
AUG06_2019	16.4	0.2	197.0	14.5	1449	-3.11	8.66
SEP16_2019	15.9	0.3	196.0	15.2	2625	-2.23	9.39
SEP24_2019	16.1	0.1	191.7	14.8	1128	-3.05	11.35
OCT16_2019	16.5	0.1	190.2	15.7	2494	-4.77	12.16
AUG22_2020	16.3	0.2	194.9	14.6	1155	-3.00	10.02
SEP05_2020	17.1	0.1	194.9	14.4	1366	-3.56	8.34

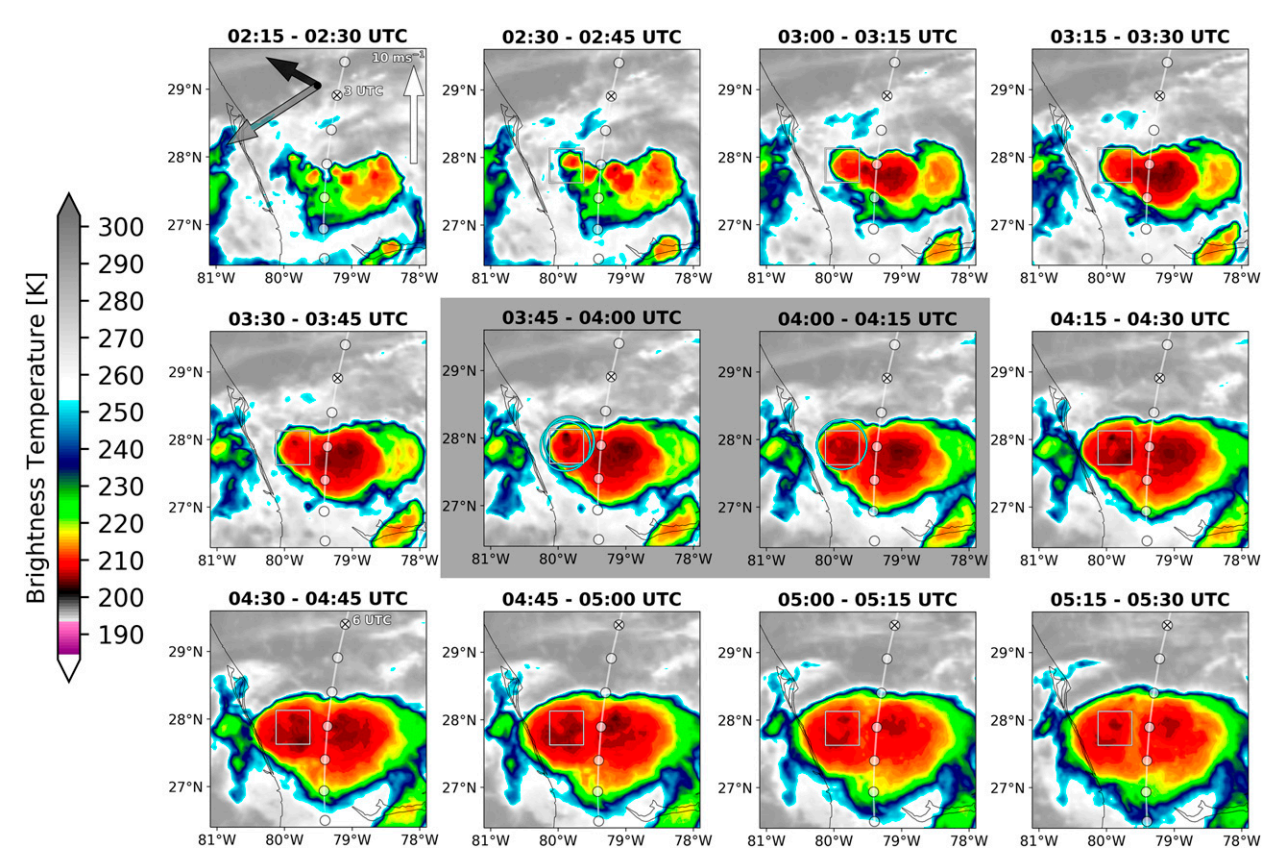


Fig. 10. As in Fig. 4, but for GOES-13 band 4 brightness temperatures (K) for TD Dorian (3 Aug 2013). GJ event (cyan rings) locations are from Lazarus et al. (2015).

particularly relevant because the convection is associated with a weak tropical disturbance/brief tropical depression off the southeast Florida coast (several sprites but no GJs were observed). While the Null3 environment is characterized by a relatively deep troposphere in the ERA5 (15.8 km), it has a diffuse and comparatively low shear (8.6 m s<sup>-1</sup>).

The corresponding observed soundings are also shown (Fig. 14). Given the location of the convection, the 0900 UTC Dorian upper-air profile (KXMR) is likely the most representative of the GJ soundings shown. Although the Dorian tropopause is somewhat warmer than the Harvey and Hilda profiles, it stands out from its ERA5 counterpart (Fig. 13a) as the tropopause is significantly sharper. The observed tropopause height is also substantially higher than the ERA5 estimate (16.5 vs 15.3 km). Given the better resolution of the observed soundings, the UTLS lapse rate differential is shown for  $\pm 2$  km of the tropopause (Table 7). The observed UTLS static stability difference is about twice that of the ERA5 and is the largest (12.9°C km $^{-1}$ ) of all the storm environments with the exception of the 24 September 2019 GJ convection.

#### 4. Discussion

Relatively small changes in wind speed ( $\Delta V$  on the order of 5–10 m s<sup>-1</sup>) above the convection can induce a critical level

(Lane et al. 2003). All of the ambient UTLS profiles shown here have layers where  $\Delta V$  is greater than 5 m s<sup>-1</sup> (Figs. 13b, 14b). Recent studies have linked frequent GW breaking (rather than storm-top divergence, flow deformation and/or stretching) near the OT to AACPs and corresponding large vector differences between the storm motion and the environmental wind in the UTLS (Homeyer et al. 2017). Lane et al. (2003) discuss two principal regions of turbulence—one of which remains local to the cloud top and a second that involves lower-stratospheric GW breaking. Lane and Sharman (2008) indicate that the above-cloud wind shear, especially the depth of the shear layer, is important. Using a storm-relative reference frame, they hypothesize that downshear-propagating gravity waves are the source of the above-cloud turbulence generation as they interact with a critical level and break. For higher shear, the critical layer is closer to the wave source thereby resulting in more intense and local wave breaking near storm top.

Here, the presence of GW breaking is inferred indirectly through the IR images which contain ringlike features and enhanced-V signatures (section 3b). Given that GJs are relatively rare, yet turbulence-generating mechanisms at storm top (gravity waves, shear, horizontal vortex generation; Lane et al. 2003) are fairly common suggests that GJs likely result from a combination of factors. For example, it is interesting to note

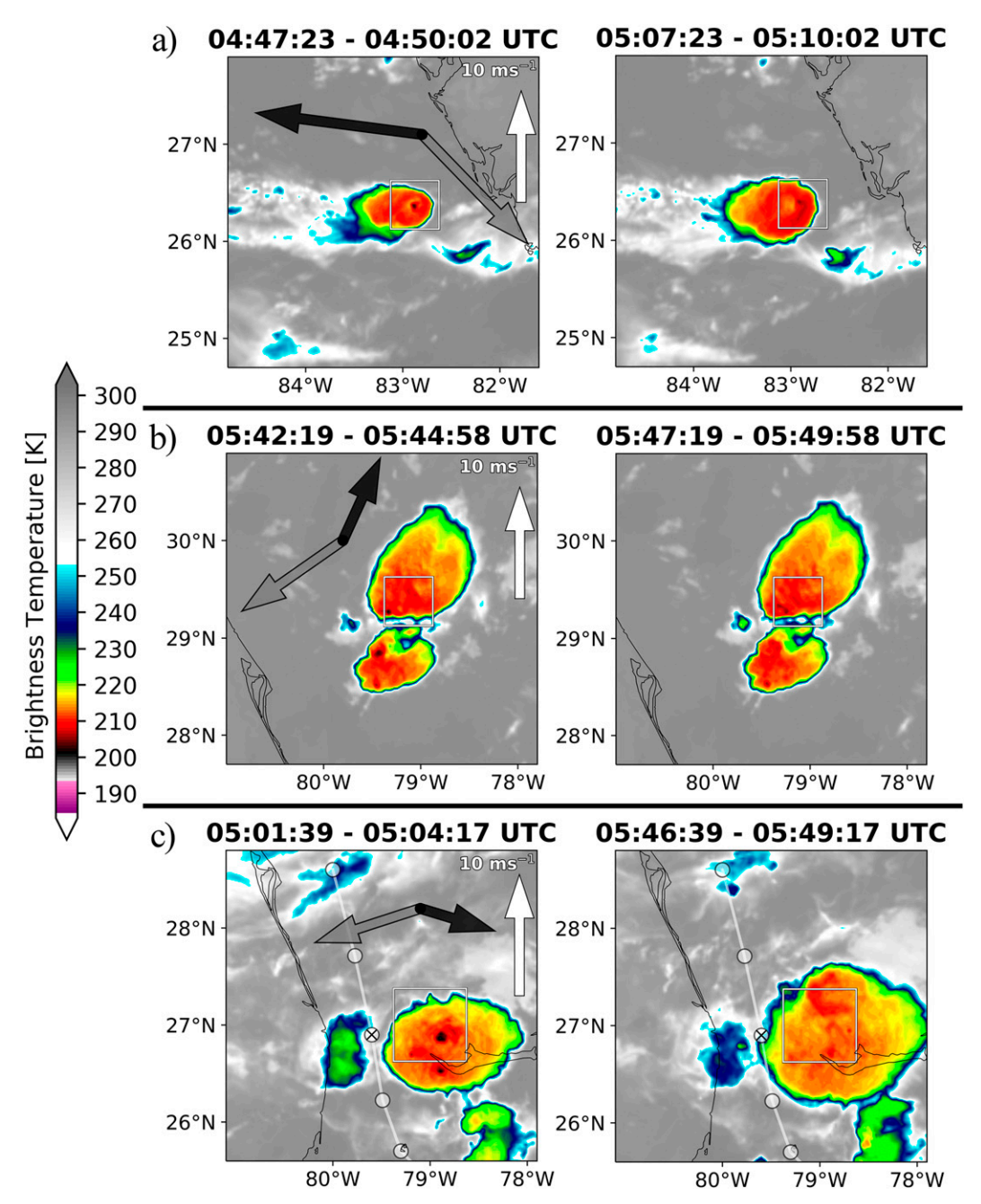
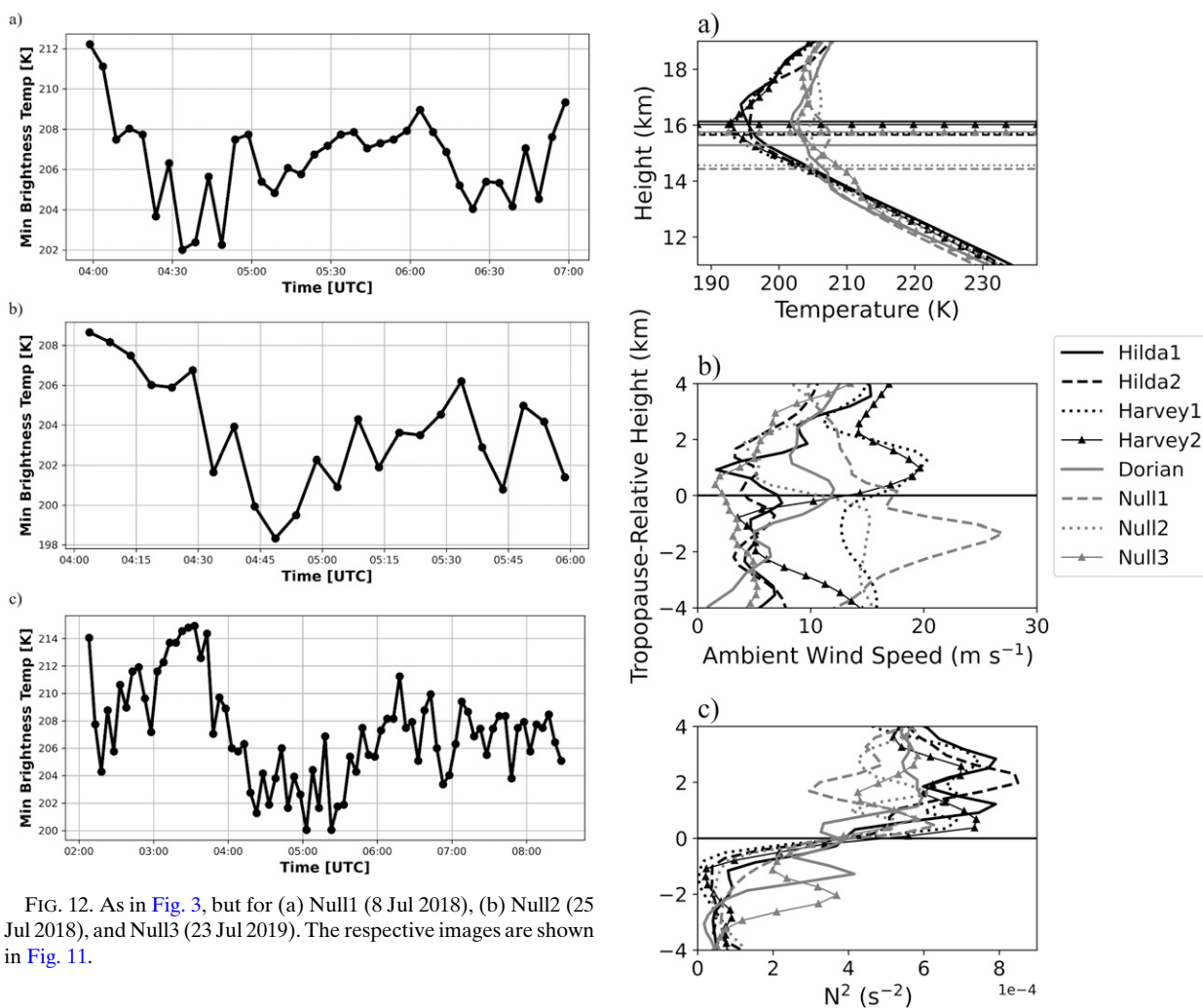


FIG. 11. As in Fig. 4, but for GOES-16 band 13 brightness temperature (K) for (a) Null1, (b) Null2, and (c) Null3 storms (8 Jul 2018, 25 Jul 2018, and 23 Jul 2019, respectively).

that, with the exception of Dorian and the Harvey rainband storms, the minimum BTs for the null storms are much warmer (by about 11°C on average, Table 4). The mean tropopause altitude is ~1.0 km higher in the TC GJ environment which is consistent with the colder mean tropopause temperatures (on the order of the 10°C, Tables 6 and 7). The relationship between GJs and deep (tall) convection is well documented in the literature (Pasko et al. 2002; Su et al. 2003; van der Velde et al. 2007; Soula et al. 2011; Meyer et al. 2013). Hence, that

tropopause height might be a good predictor of GJ producing thunderstorms is not all that surprising. The connection between a deep troposphere and storm-top turbulence generation was first addressed by Krehbiel et al. (2008). Using an idealized charging model, they linked the rate of dissipation of the upper positive charge region, via Maxwellian relaxation, to altitude whereby storm-top mixing is modeled by increased electrical conductivity. In the upper portions of the cloud, the conductivity is assumed to increase exponentially across the



cloud boundary, from zero within the cloud to values equal to the pristine air above the storm. Because conductivity increases with altitude, taller storms will more quickly dilute the upper charge reservoir (relative to the lower reservoir) hastening the charge imbalance (the rate at which the screening layer forms at storm top is inversely proportional to the conductivity above cloud top). In addition to the role of electrical conductivity with altitude, GW disturbances tend to increase in amplitude as a result of decreasing atmospheric density (Fritts and Alexander 2003; Costantino et al. 2015). Hence, the tropopause connection to GJs and storm-top turbulence is actually twofold, i.e., 1) directly through enhancing the intensity of GW breaking due to the decrease in density (all things being equal) and 2) indirectly as a result of changes in the electrical conductivity. In terms of the latter, assuming an exponential conductivity increase with height above cloud top and a scaling altitude of 6 km (Riousset et al. 2010), the conductivity at the tropopause increases by a factor of 1.3 between the Null1 and Harvey2 environments. This results in about a 4-s difference (decrease) in the screen-layer formation time scale in these two environments (16.1 vs 12.1 s, respectively). This assumes that the lower charge reservoir is not displaced upward, which

FIG. 13. (a) UTLS temperature (K), tropopause-relative (b) ambient wind speed profiles (m s<sup>-1</sup>), and (c) Brunt-Väisälä frequency squared (s<sup>-2</sup>). Profiles shown are the means for each level, obtained from the ERA5 spatiotemporal footprints (see text and online supplementary material for details). Also shown in (a) are the corresponding mean tropopause heights (horizontal lines), which share the same legend as the profiles. The tropopause levels are defined using the WMO 1957 definition.

would also increase the dissipation rate of the lower charge region. In the absence of a four-dimensional lightning surveillance system (e.g., lightning detection and ranging) this information is not available except for Dorian (e.g., see Boggs et al. 2018). Storm electrification issues, such as the shutdown hypothesis (i.e., the lull of negative cloud-to-ground flashes; van der Velde et al. 2007), are not addressed here.

It is also instructive to look at less prodigious (LP) GJ events in the region. As such, an additional six events from 2019 to 2020 are included in Tables 5-7. Five of these storms were observed by the low-light camera in SW Puerto Rico and one (16 October 2019) was observed by a commercial pilot northwest of the Yucatan Peninsula over the south-central Gulf of

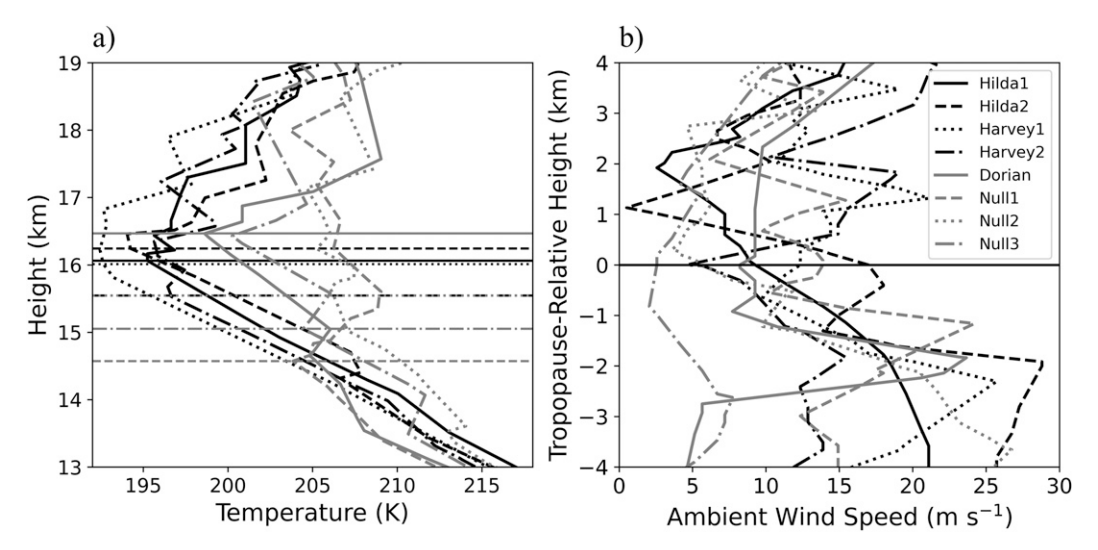


FIG. 14. As in Figs. 13a and 13b, but for the observed proximity soundings: Hilda1 (PHTO, 0600 UTC 11 Aug 2015), Hilda2 (PHTO, 1200 UTC 12 Aug 2015), Harvey1 (TNCC, 0000 UTC 19 Aug 2017), Harvey2 (TJSJ, 1200 UTC 19 Aug 2017), Dorian (XMR, 0900 UTC 3 Aug 2013), Null1 (TBW, 0000 UTC 9 Jul 2018), Null2 (JAX, 0000 UTC 26 Jul 2018), and Null3 (KMLB, 0900 UTC 23 Jul 2019).

Mexico. According to NHC surface analyses, three of these occurred in conjunction with tropical waves moving through the central Caribbean, two were produced by weak TCs (Karen and Laura), and one (Yucatan) was associated with an inverted trough. With the exception of 5 September 2020, for which there were three GJs observed, the others were single events. Using the ERA5, the lower (4 km)-stratospheric lapse rates are plotted versus the maximum tropopause wind shear magnitude in Fig. 15. Three groupings are shown, i.e., the nulls, the multi-GJ event TCs (Hilda, Harvey, and Dorian) and the 2019–20 GJs. While the range in tropopause shear is comparable, the stratosphere is more stable in the GJ cases with the exception of TD Dorian. That Dorian appears to be an outlier may be a combination of the averaging (i.e., mean ERA5 profiles), the presence of a very sharp tropopause, and a narrow upper-level deformation zone (Fig. 2, Lazarus et al. 2015). The observed tropopause height from the XMR sounding (0900 UTC 3 August 2013, Table 7) is 1.2 km higher than the ERA5, and the lower-stratospheric stability has an observed lapse rate of  $-9.4 \,\mathrm{K \, km^{-1}}$  (the ERA5 lapse rate is  $-1.2 \,\mathrm{K \, km^{-1}}$ ). The discrepancy between the observed and ERA5 lower-stratospheric lapse rates for Dorian is, by far, the largest of the 14 environments. The tropopause heights, when averaged separately for the three groups (i.e., multi-GJ, LP GJ and Nulls) the ERA5 and observed tropopause heights are within 200–300 m of one another (not shown)—comparable to the spread  $(\pm 1 \sigma)$  of the ERA5 sampled profiles (Table 6). What is interesting, however, is that despite the small spatiotemporal footprint for Dorian (0.25° latitude-longitude box and 2-h window), the variability in the tropopause height estimate is quite high ( $\pm 700 \,\mathrm{m}$ ); the largest of the ERA5 footprints. The shallow shear layer near the observed tropopause  $(18 \,\mathrm{m \, s^{-1}}$  over 900-m layer, Table 5; Lazarus et al. 2015; and Fig. 14b) is also poorly resolved in the ERA5 ( $11.5 \,\mathrm{m \, s^{-1}}$ , Table 5 and Fig. 13b). Despite the relatively high vertical resolution of the ERA5 near the tropopause, the presence of distinct boundaries such as Dorian's is problematic. Nonetheless, the ERA5 is consistent with respect to the observed soundings and minimum BTs (Tables 4 and 6)—the latter of which indicates that Dorian has the warmest cloud tops of the TC GJ environments. It may be that storm-top shear is more important in these cases by compensating for a lower tropopause as a significant turbulence source in a role akin to the "jet-width" issue (described previously) where the GW breaking is more intense and occurs closer to cloud top (i.e., shear-layer depth; Lane and Sharman 2008). The shear layer may also play an important role by increasing the likelihood of inducing a critical level and GW breaking (Lane et al. 2003).

While it is important to characterize the convection, radar estimates of the storm-top heights can be problematic in remote locations. Here, reflectivity is available for Hilda2, Harvey rainband GJs (11, 17, and 18, Table 2), Dorian, and the null cases. Table 8 lists radar estimates of the beamwidth (top/bottom/center) and corresponding range for the uppermost tilt. The spread and range are approximately 2.5 and 81 km, respectively, for Dorian, whereas they are greater than 7 and 451 km, respectively, for Hilda2. If one assumes that the center beam is representative of storm top, then all but the last two Harvey events (which had the warmest local BTs of the GLM-identified GJs) appear to be associated with tropopause penetrating convection. However, because of the overlap in the tilts as a result of the beam spreading, there is considerable uncertainty in the actual storm-top heights. For example, the beam height and corresponding maximum reflectivity for the 0725 UTC Harvey storm (referred to as HA1) appear to be on the high side (17.8 km and 21 dBZ, respectively) when compared to the later (0846 UTC) rainband storm (referred to as HA2) that produces GJ events 17 and 18 (15.2 km and 33 dBZ). In addition, the local minimum brightness temperature is actually warmer, by 2 K, for the former. The maximum vertical

TABLE 7. Observed thermodynamic quantities obtained from proximity upper-air soundings (Fig. 14) including the event, sounding location, date and time, tropopause (trop) height and temperature (temp), minimum (Min) temperature (cold point), lower-stratospheric lapse rates ( $\Gamma$ , tropopause to 2 km above), and the lapse-rate differences ( $\Delta\Gamma$ ) estimated for the layer  $\pm 2$  km of the tropopause.

Event	Location	Date	Time (UTC)	Trop height (km)	Trop temp (K)	Min temp (K)	$Trop + 2 km \Gamma$ $(K km^{-1})$	$\Delta\Gamma$ $(K \text{ km}^{-1})$
Null1	TBW	9 Jul 2018	0000	14.6	203.8	203.6	-1.4	5.9
Null2	JAX	26 Jul 2018	0000	15.5	206.2	204.6	-1.3	5.3
Null3	XMR	23 July 2019	0900	15.1	204.4	200.2	-0.1	4.1
Hilda1	PHTO	11 Aug 2015	0600	16.1	195.2	195.2	-3.0	10.5
Hilda2	PHTO	12 Aug 2015	1200	16.2	194.2	194.0	-4.8	11.3
Harvey1	TNCC	19 Aug 2017	0000	16.0	192.6	192.4	-2.0	9.6
Harvey2	TJSJ	19 Aug 2017	1200	15.5	196.6	195.6	-0.3	7.9
Dorian	XMR	3 Aug 2013	0900	16.5	198.6	198.6	-9.4	12.9
AUG06_2019	MDSD	6 Aug 2019	1200	15.8	201.2	196.8	-0.1	3.0
SEP16_2019	TJSJ	16 Sep 2019	0000	15.9	197.6	195.4	1.4	3.5
SEP24_2019	TJSJ	24 Sep 2019	0000	16.6	189.2	189.2	-7.1	13.5
OCT16_2019	MZBZ	16 Oct 2019	1200	16.4	191.6	191.6	-4.0	9.6
AUG22_2020	TJSJ	22 Aug 2020	1200	15.3	199.6	196.2	2.0	3.9
SEP05_2020	TJSJ	5 Sep 2020	1200	16.7	195.6	195.4	-2.9	7.8

reflectivity gradient for Dorian, which is well sampled near the storm top, decreases on the order of 10–15 dBZ km<sup>-1</sup> between the 10° and 12° tilts (Lazarus et al. 2015, Fig. 14). Using the lower (conservative) estimate for the lapse rate (-10 dBZ)km<sup>-1</sup>), the maximum reflectivity (33 dBZ) for HA2 can be extrapolated upward to match that of HA1 (21 dBZ)—which would place the storm top closer to 16.4 km or about 1.2 km higher than the center beam height estimate. This level is also likely a better estimate of the storm-top height for HA1, i.e., 1.4 km below the beam center but still above the beam bottom (15.8 km). The overlap due to the beam spreading, which ranges from 15.8 to 17.4 km (1.6 km), is shown in Fig. 16 (as a vertical bar and whiskers). Similarly, the Hilda2 maximum reflectivity is quite large (47 dBZ)—as even for the most intense of oceanic convection it is rare for reflectivity to exceed 40 dBZ at altitudes above 10 km (Kumar and Bhat 2016). Given the high reflectivity and considerable beam spreading at this range, the storm top is also likely below the beam center height for this case as well. The differences between the unadjusted storm-top and tropopause height (a proxy for overshoot depth) are given in Table 8. Note, however, that the differences in the tropopause penetration, which is greater for two of the null storms compared to the GJ convection, would be even larger if these downward adjustments were made (assuming that the null storm tops are representative).

Figure 16 illustrates the composite storm-top characteristics (from the radar, ERA5, and observed soundings) for the GJ versus null storm environments. The heights (and relative distances) shown are with respect to the mean tropopause levels for the GJ and null storm environments (15.8 and 14.9 km, respectively). As previously mentioned, the observed soundings (Fig. 14) are similar with the GJ (null) tropopause level at 16.1 km (15.1 km). The radar-estimated maximum storm-top height, depicted as OTs in Fig. 16, indicates that, after adjusting for HA1, the Null1 and Null2 storms appear to have deeper stratospheric penetration. The increased penetration depth is consistent with the lower static stability,

higher (average) most unstable (MU) CAPE of 2060 J kg<sup>-1</sup> (vs 1613 J kg<sup>-1</sup> for the GJ storms and 1703 J kg<sup>-1</sup> for the 2019–20 GJ storms, Table 6) and diffuse tropopause. In general, the CAPE tends to be lower in tropical cyclone environments (Molinari et al. 2012). This scenario, in tandem with the reduced overshoot depth may be more favorable for repeated tropopause penetrations (i.e., OT gravity wave source/oscillation mechanism) that have been associated with the development of cold rings versus ephemeral stratospheric intrusions that might otherwise produce the more common

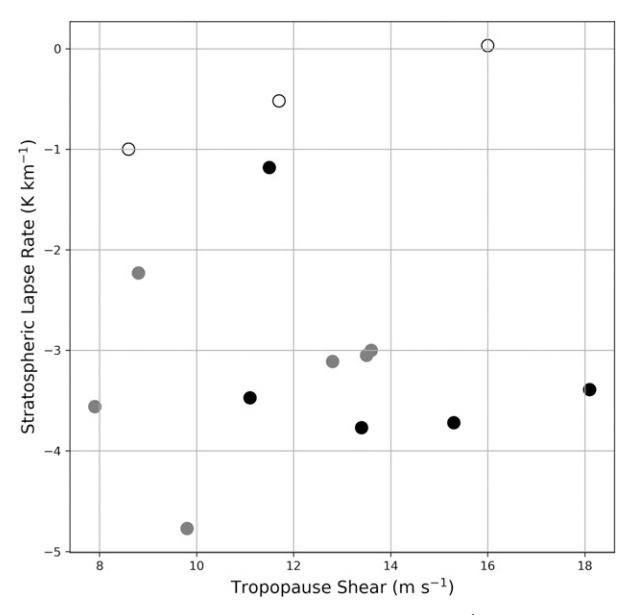


FIG. 15. ERA5 stratospheric lapse rates (K km<sup>-1</sup>, Table 6) vs the tropopause shear (m s<sup>-1</sup>, Table 5). The open circles represent the null cases, the filled black circles depict the multi-TC GJ events (Hilda, Harvey, and Dorian), and the filled gray circles are the 2019–20 GJ events.

TABLE 8. Radar storm-top data (obtained from the highest tilt with reflectivity) at the time of peak storm intensity (determined using the maximum echo-top height). Also shown is the ERA5 penetration depth, i.e., difference between the central beam height and tropopause (trop) levels. HA1 and HA2 represent the two Harvey rainband storms (see Table 2). Scan time shown is for the storm-top tilt.

Event	Site	Time	Central beam height (km)	Top (km)	Bottom (km)	Storm top – trop (km)	Z (dB $Z$ )	Tilt (°)	Range (km)	Azimuth (°)
Hilda2	PHWA	1242 UTC 12 Aug 2015	15.9	19.7	12.4	0.2	47.0	0.5	451.3	109.5
HA1 725 UTC	TJUA	0722 UTC 19 Aug 2017	17.8	19.8	15.8	1.9	21.0	3.4	240.6	159.5
HA2 846 UTC	TJUA	0847 UTC 19 Aug 2017	15.2	17.4	13.0	-0.7	33.0	2.4	260.4	206.5
Dorian	<b>KMLB</b>	0359 UTC 3 Aug 2013	14.8	16.2	13.8	-0.5	36.0	10.0	81.3	101.5
Null1	KTBW	0449 UTC 9 Jul 2018	16.3	18.2	14.7	1.9	35.5	5.1	165.2	196.5
Null2	<b>KMLB</b>	0453 UTC 26 Jul 2018	16.6	18.6	15.1	2.0	34.0	4.0	202.8	44.5
Null3	KAMX	0501 UTC 23 Jul 2019	16.6	18.8	14.5	0.8	20.5	4.0	200.9	49.5

EWS or the more extensive overshoots associated with AACPs (e.g., Homeyer et al. 2017).

Using reanalysis data, Splitt and Lazarus (2017) examined the skill of various large-scale variables in predicting occurrence of 28 global GJ events spanning 17 years. The variables included precipitable water, cloud water, tropopause shear, low-level absolute vorticity, CAPE, 0-3-km SRH, and freezing level. The combination that maximized (minimized) hits (false alarms) was the threshold selection for CAPE and SRH. Most, but not all, of the GJs were over water and many were associated with tropical disturbances. Bedka et al. (2018) have shown that a defining characteristic for AACP-producing storms is that the deep tropopause-penetrating updrafts are rotating at the time of AACP production. While the maximum SRH is elevated in our TC GJ cases, the low SRH in the 2019-20 pool of LP GJ environments, which is comprised of three tropical waves and two TCs (Table 5), suggests that the increased predictive skill may indeed be attributed to tropical storms in general, which tend to have elevated SRH, especially when compared to the null environments. Studies have shown that the SRH is significantly enhanced in the downshear (with respect to the 850-200-hPa shear vector) quadrants of tropical cyclones (Molinari and Vollaro 2010). This may explain, in part, why the Dorian GJs occur in the left-rear quadrant with respect to storm motion as it is the downshear direction with respect to the deep-layer shear vector (Fig. 10).

Interestingly, the upper-level storm environment for GJs appears to be different from that of the AACP in that the latter favors lower-stratospheric stability and a more diffuse tropopause (Homeyer et al. 2017). This suggests that GW breaking may be more constrained to the cloud top near the OT in the GJ environment compared to jumping cirrus and AACPs, where stratospheric wave breaking extends over a deeper layer (Wang 2007). In their two-dimensional simulations, Lane and Sharman (2008) show a highly localized region of intense turbulence along and near the cloud-top edge in association with strong wind shear (they attribute the turbulence in this case to flow deformation rather than GW breaking). While this may be an important factor in cases with a lower tropopause, our results indicate that high ambient shear layers near storm top are not necessarily a requisite for TC-related GJs. Furthermore, although the lower-stratospheric stability was varied between their simulations, it is assumed to be constant with height. As shown here, this is certainly not the case in the GJ or null environments (Fig. 13c). More importantly, the sharp increase in the static stability near the tropopause of the GJ environments

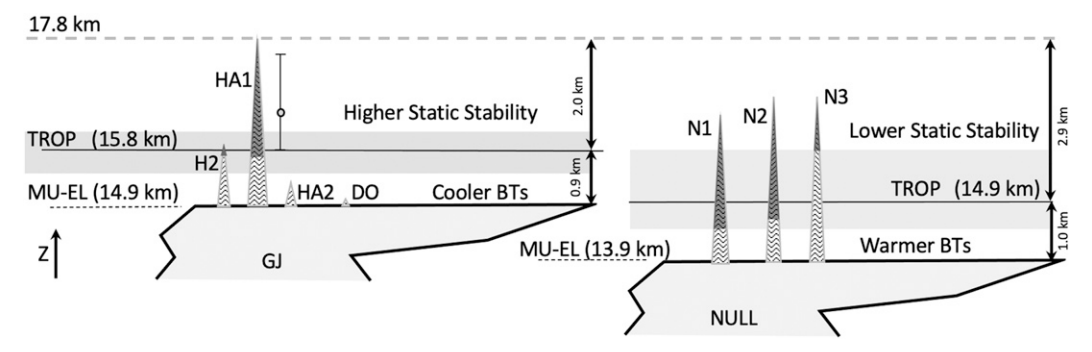


FIG. 16. Combined ERA5 and radar storm-top characteristics for (left) TC GJs and (right) null storms. Shown are the mean tropopause heights (TROP; solid horizontal lines) and range (shaded region above the storm top), the most unstable equilibrium level (MU-EL; dotted lines) and radar-estimated storm-top heights for H2 (Hilda night 2), HA1 and HA2 (Harvey rainband storms associated with GJs 11 and 17/18, respectively), Dorian (DO), and null storms (Null1—N1; Null2—N2; and Null3—N3). The portion of the overshoot above each storm's respective ERA5 tropopause level (i.e., the penetration depth) is indicated by the dark gray shading of the peaks. The circle, vertical bar, and whiskers represent an adjusted estimate of the storm-top heights and vertical extent of the overlap in the radar beams for HA1 and HA2 (see text for details and Tables 7 and 8 for specific numbers).

TABLE 9. Event checklist for ambient/storm thresholds and storm features. Quantities listed include the brightness temperature minimum (BT $_{min}$ ), ERA5 tropopause (Trop) height, the observed (obs) upper-tropospheric–lower-stratospheric lapse-rate difference (UTLS LR  $\pm$  2 km tropopause), and UTLS maximum (max) shear ( $\pm$ 4 km tropopause). Also shown is the average ranking (based on the first four parameters), penetration depth (difference between the radar storm-top estimate and ERA5 tropopause height), and satellite features. The ranking (which ranges from 1 to 8) indicates where the events (Hilda, Harvey, Dorian, and Nulls) fall with respect to the parameter thresholds listed (see text for details).

Parameter/feature	Hilda1	Hilda 2	Harvey1	Harvey2	Dorian	Null1	Null2	Null3
$BT_{min} < 195 \text{ K}$	×	×	X	X				×
Trop height $> 15 \mathrm{km}$	×	×	×	×	×			
UTLS LR (obs) $> 7 \mathrm{K  km^{-1}}$	×	×	×	×	×			
UTLS max shear (obs) $> 0.02 \mathrm{s}^{-1}$	×	×	×	×	×			
Average ranking	2.8	2.5	3.0	3.8	3.8	7.0	6.8	6.5
Penetration depth < 2 km	×	×		×	×			×
Cold ring/CWS		×	×					×
Enhanced V	×							
EWS/EWA			×	×	×	×	×	×

herein supports a GW source (i.e., the OT) with increased amplitude, wave breaking and enhanced storm-top turbulence.

#### 5. Conclusions

Satellite images indicate that GJs were observed in environments that include cold rings, enhanced V, and EWS. Although these features may be indicative of storm-top turbulence, their presence alone does not necessarily guarantee GJs as the null storms also have downwind warm spots and/or warm areas. While overshoots, storm-top divergence, and gravity waves are ubiquitous signatures of deep convection, when compared to the null convection, the tropical cyclone GJ environment has, in general, a higher tropopause, and more stable stratosphere (as a result, the  $N^2$  and stratospheric lapse rates are steeper for the GJ storms—resulting in a sharper more well-defined tropopause). A summary checklist of storm and ambient characteristics are provided in Table 9. Albeit somewhat arbitrary, the thresholds selected are not intended to be a hard yes or no with respect to GJ occurrence nor should they be taken individually. The ranking, which ranges from 1 to 8, represents an average over the four leading parameters. The GJ (null) environments are similar with a relatively large gap between the two groups. The advantage of a higher tropopause is that both electrical conductivity and GW breaking increase with altitude and thus act in tandem to promote charge dilution by both increasing the rate at which the screening layer forms and enhancing the storm-top mixing. In general, the combination of a higher tropopause, reduced penetration depth and more distinct tropopause may support a scenario in which the GW breaking is enhanced near the cloud top in the GJ environment. The UTLS shear may be more important in cases with a lower tropopause (e.g., TD Dorian), by increasing the likelihood of inducing a critical level and/or increasing the amplitude of GW breaking/turbulence.

Understanding the nuances of storm-top structure [tropopause, wind shear, storm-relative flow (SRF)] ultimately requires detailed model simulations in part because the ambient environment is significantly impacted/modified by the convection itself. With the exception of the screening layer, we have deliberately avoided links between storm structure and electrification

issues such as the microphysics and charge separation. Despite the lack of LMA data, there are some insights that could be gleaned from the Advanced Baseline Imager (ABI), especially in the shortwave. Additional null cases, especially tropical systems might be more revealing—but are difficult to ascertain. Regardless, a broad overview of what the undisturbed TC GJ environment looks like establishes a framework for numerical simulations as well as future field campaigns.

Acknowledgments. This unfunded project would not have been possible without the Florida Tech Geospace Physics Lab, under the supervision of Dr. Amitabh Nag, which provided the low-light camera data for the null events. A note of sincere appreciation is also extended to Frankie Lucena, an amateur photographer located in SW Puerto Rico, for the spectacular images of the Harvey GJs and the sharing of data from many other events as well. JAR's contribution to this material is based upon work supported by the National Science Foundation under Grant No. 2047863 to Florida Institute of Technology.

Data availability statement. All satellite data (IR and GLM) are openly available through the NOAA CLASS server at https://www.bou.class.noaa.gov/saa/products/welcome. The GLM identified GJ locations are published in the literature and are included in Boggs et al. (2019). National Weather Service radar data are also freely available via direct download at https:// www.ncdc.noaa.gov/nexradinv/map.jsp or through Amazon Web Services at https://s3.amazonaws.com/noaa-nexradlevel2/index.html. Upper-air observations are available online at http://weather.uwyo.edu/upperair/sounding.html. The ERA5 dataset is also public domain and available at https:// www.ecmwf.int/en/forecasts/datasets/reanalysis-datasets/era5. The official NHC best track dataset (IBTrACS) can be downloaded from https://doi.org/10.25921/82ty-9e16 and is referenced herein (Knapp et al. 2010, 2018). Camera data (video) for the Harvey GJs are viewable online at https://www.youtube.com/ watch?v=90s-2RSuhQs and Hilda time lapse from the Hawaii observatory (CFHT CloudCam on Mauna Kea) is posted at https://www.youtube.com/watch?v=3p\_WDUEselE&ab\_channel= FrankieLucena.

#### REFERENCES

- Bedka, K., E. M. Murillo, C. R. Homeyer, B. Scarino, and H. Mersiovsky, 2018: The above-anvil cirrus plume: An important severe weather indicator in visible and infrared satellite imagery. Wea. Forecasting, 33, 1159–1181, https:// doi.org/10.1175/WAF-D-18-0040.1.
- Beres, J. H., M. J. Alexander, and J. R. Holton, 2002: Effects of tropospheric wind shear on the spectrum of convectively generated gravity waves. *J. Atmos. Sci.*, 59, 1805–1824, https://doi.org/ 10.1175/1520-0469(2002)059<1805:EOTWSO>2.0.CO;2.
- Blake, E. S., and J. Jelsema, 2016: Hurricane Hilda (EP102015): 6– 13 August 2015. National Hurricane Center Tropical Cyclone Rep., 16 pp.
- ——, and D. A. Zelinsky, 2018: Hurricane Harvey (AL092017): 17 August–1 September 2017. National Hurricane Center Tropical Cyclone Rep., 16 pp.
- Boggs, L. D., N. Liu, J. A. Riousset, F. Shi, S. Lazarus, M. Splitt, and H. Rassoul, 2018: Thunderstorm charge structures producing gigantic jets. Sci. Rep., 8, 18085, https://doi.org/10.1038/ s41598-018-36309-z.
- —, M. Peterson, S. Lazarus, M. Splitt, F. Lucena, A. Nag, and H. Rassoul, 2019: First observations of gigantic jets from geostationary orbit. *Geophys. Res. Lett.*, 46, 3999–4006, https://doi.org/10.1029/2019GL082278.
- Chen, A. B., and Coauthors, 2008: Global distributions and occurrence rates of transient luminous events. *J. Geophys. Res.*, 113, A08306, https://doi.org/10.1029/2008JA013101.
- Costantino, L., P. Heinrich, N. Mze, and A. Hauchecorne, 2015: Convective gravity wave propagation and breaking in the stratosphere: Comparison between WRF Model simulations and lidar data. *Ann. Geophys.*, 33, 1155–1171, https://doi.org/ 10.5194/angeo-33-1155-2015.
- Dauhut, T., J.-P. Chaboureau, P. H. Haynes, and T. P. Lane, 2018: The mechanisms leading to a stratospheric hydration by overshooting convection. *J. Atmos. Sci.*, **75**, 4383–4398, https://doi.org/10.1175/JAS-D-18-0176.1.
- Duran, P., and J. Molinari, 2016: Upper-tropospheric low Richardson number in tropical cyclones: Sensitivity to cyclone intensity and the diurnal cycle. *J. Atmos. Sci.*, 73, 545–554, https://doi.org/ 10.1175/JAS-D-15-0118.1.
- Fovell, R., D. Durran, and J. R. Holton, 1992: Numerical simulations of convectively generated stratospheric waves. *J. Atmos. Sci.*, **49**, 1427–1442, https://doi.org/10.1175/1520-0469(1992) 049<1427:NSOCGS>2.0.CO;2.
- Fritts, D. C., and M. J. Alexander, 2003: Gravity wave dynamics and effects in the middle atmosphere. Rev. Geophys., 41, 1003, https://doi.org/10.1029/2001RG000106.
- Fujita, T. T., 1982: Principle of stereoscopic height computations and their applications to stratospheric cirrus over severe thunderstorms. J. Meteor. Soc. Japan, 60, 355–368, https:// doi.org/10.2151/jmsj1965.60.1\_355.
- Gavrilov, N. M., and S. Fukao, 2004: Numerical and the MU radar estimations of gravity wave enhancement and turbulent ozone fluxes near tropopause. *Ann. Geophys.*, 22, 3889–3898, https:// doi.org/10.5194/angeo-22-3889-2004.
- Grabowski, W. W., and T. L. Clark, 1991: Cloud–environment interface instability: Rising thermal calculations in two spatial dimensions. J. Atmos. Sci., 48, 527–546, https://doi.org/10.1175/ 1520-0469(1991)048<0527:CIIRTC>2.0.CO;2.
- Helmus, J. J., and S. M. Collis, 2016: The Python ARM Radar Toolkit (Py-ART), a library for working with weather radar data in the Python programming language. *J. Open Res. Software*, **4**, e25, https://doi.org/10.5334/jors.119.

- Hersbach, H., and Coauthors, 2020: The ERA5 global reanalysis. *Quart. J. Roy. Meteor. Soc.*, **146**, 1999–2049, https://doi.org/10.1002/qj.3803.
- Heymsfield, G. M., R. H. Blackmer, and S. Schotz, 1983: Upper-level structure of Oklahoma tornadic storms on 2 May 1979. I: Radar and satellite observations. *J. Atmos. Sci.*, 40, 1740–1755, https:// doi.org/10.1175/1520-0469(1983)040<1740:ULSOOT>2.0.CO;2.
- Homeyer, C. R., J. D. McAuliffe, and K. M. Bedka, 2017: On the development of above-anvil cirrus plumes in extratropical convection. *J. Atmos. Sci.*, 74, 1617–1633, https://doi.org/ 10.1175/JAS-D-16-0269.1.
- Knapp, K. R., M. C. Kruk, D. H. Levinson, H. J. Diamond, and C. J. Neumann, 2010: The International Best Track Archive for Climate Stewardship (IBTrACS): Unifying tropical cyclone best track data. *Bull. Amer. Meteor. Soc.*, 91, 363–376, https://doi.org/10.1175/2009BAMS2755.1.
- ——, H. J. Diamond, J. P. Kossin, M. C. Kruk, and C. J. Schreck, 2018: International Best Track Archive for Climate Stewardship (IBTrACS) project, version 4. NOAA National Centers for Environmental Information, accessed 5 April 2020, https:// doi.org/10.25921/82ty-9e16.
- Krehbiel, P. R., J. A. Riousset, V. P. Pasko, R. J. Thomas, W. Rison, M. A. Stanley, and H. E. Edens, 2008: Upward electrical discharges from thunderstorms. *Nat. Geosci.*, 1, 233– 237, https://doi.org/10.1038/ngeo162.
- Kumar, S., and G. S. Bhat, 2016: Vertical profiles of radar reflectivity factor in intense convective clouds in the tropics. J. Appl. Meteor. Climatol., 55, 1277–1286, https://doi.org/10.1175/JAMC-D-15-0110.1.
- Lane, T. P., and R. D. Sharman, 2008: Some influences of background flow conditions on the generation of turbulence due to gravity wave breaking above deep convection. *J. Appl. Meteor. Climatol.*, 47, 2777–2796, https://doi.org/ 10.1175/2008JAMC1787.1.
- —, —, T. L. Clark, and H.-M. Hsu, 2003: An investigation of turbulence generation mechanisms above deep convection. J. Atmos. Sci., 60, 1297–1321, https://doi.org/10.1175/1520-0469(2003)60<1297:AIOTGM>2.0.CO:2.
- —, —, S. B. Trier, R. G. Fovell, and J. K. Williams, 2012: Recent advances in the understanding of near-cloud turbulence. *Bull. Amer. Meteor. Soc.*, **93**, 499–515, https://doi.org/10.1175/BAMS-D-11-00062.1.
- Lazarus, S. M., M. E. Splitt, J. Brownlee, N. Spiva, and N. Liu, 2015: A thermodynamic, kinematic and microphysical analysis of a jet and gigantic jet-producing Florida thunderstorm. *J. Geophys. Res. Atmos.*, 120, 8469–8490, https://doi.org/ 10.1002/2015JD023383.
- Lindsey, D. T., and M. J. Bunkers, 2005: Observations of a severe, left-moving supercell on 4 May 2003. Wea. Forecasting, 20, 15– 22, https://doi.org/10.1175/WAF-830.1.
- Liu, N., N. Spiva, J. R. Dwyer, H. K. Rassoul, D. Free, and S. A. Cummer, 2015: Upward electrical discharges observed above Tropical Depression Dorian. *Nat. Commun.*, 6, 5995, https://doi.org/10.1038/ncomms6995.
- Luderer, G., J. Trentmann, K. Hungershofer, M. Herzog, and M. Fromm, and M. O. Andreae, 2007: Small-scale mixing processes enhancing troposphere-to-stratosphere transport by pyrocumulonimbus storms. *Atmos. Chem. Phys.*, 7, 5945–5957, https://doi.org/10.5194/acp-7-5945-2007.
- McCann, D. W., 1983: The enhanced-V: A satellite observable severe storm signature. *Mon. Wea. Rev.*, **111**, 887–894, https://doi.org/10.1175/1520-0493(1983)111<0887:TEVASO> 2.0.CO;2.

- Meyer, T. C., T. J. Lang, S. A. Rutledge, W. A. Lyons, S. A. Cummer, G. Lu, and D. T. Lindsey, 2013: Radar and lightning analyses of gigantic-jet-producing storms. *J. Geophys. Res. Atmos.*, 118, 2872–2888, https://doi.org/10.1002/jgrd.50302.
- Molinari, J., and D. Vollaro, 2010: Distribution of helicity, CAPE, and shear in tropical cyclones. *J. Atmos. Sci.*, 67, 274–284, https://doi.org/10.1175/2009JAS3090.1.
- —, D. M. Romps, D. Vollaro, and L. Nguyen, 2012: CAPE in tropical cyclones. J. Atmos. Sci., 69, 2452–2463, https://doi.org/ 10.1175/JAS-D-11-0254.1.
- ——, P. Duran, and D. Vollaro, 2014: Low Richardson number in the tropical cyclone outflow layer. *J. Atmos. Sci.*, **71**, 3164– 3179, https://doi.org/10.1175/JAS-D-14-0005.1.
- Negri, A. J., 1982: Cloud-top structure of tornadic storms on 10 April 1979 from rapid scan and stereo satellite observations. *Bull. Amer. Meteor. Soc.*, 63, 1151–1159, https://doi.org/ 10.1175/1520-0477-63.10.1151.
- Pasko, V. P., M. A. Stanley, J. D. Mathews, U. S. Inan, and T. G. Wood, 2002: Electrical discharge from a thundercloud top to the lower ionosphere. *Nature*, 416, 152–154, https://doi.org/10.1038/416152a.
- Pfister, L., and Coauthors, 1993: Gravity waves generated by a tropical cyclone during the STEP tropical field program: A case study. J. Geophys. Res., 98, 8611–8638, https://doi.org/ 10.1029/92JD01679.
- Piani, C., D. Durran, M. J. Alexander, and J. R. Holton, 2000: A numerical study of three-dimensional gravity waves triggered by deep tropical convection and their role in the dynamics of the QBO. J. Atmos. Sci., 57, 3689–3702, https://doi.org/ 10.1175/1520-0469(2000)057<3689:ANSOTD>2.0.CO;2.
- Riousset, J. A., V. P. Pasko, P. R. Krehbiel, W. Rison, and M. A. Stanley, 2010: Modeling of thundercloud screening charges: Implications for blue and gigantic jets. J. Geophys. Res., 115, A00E10, https://doi.org/10.1029/2009JA014286.
- Said, R. K., M. B. Cohen, and U. S. Inan, 2013: Highly intense lightning over the oceans: Estimated peak currents from global GLD360 observations. *J. Geophys. Res. Atmos.*, 118, 6905–6915, https://doi.org/10.1002/jgrd.50508.
- Setvák, M., and R. M. Rabin, 2003: MODIS observations of deep convective cloud tops. Proc. 2003 EUMETSAT Meteorological Satellite Conf., Weimar, Germany, EUMETSAT, 381–388.
- —, and Coauthors, 2010: Satellite-observed cold-ring-shaped features atop deep convective clouds. *Atmos. Res.*, 97, 80–96, https://doi.org/10.1016/j.atmosres.2010.03.009.
- Soula, S., O. van der Velde, J. Montanya, P. Huet, C. Barthe, and J. Bór, 2011: Gigantic jets produced by an isolated tropical thunderstorm near Réunion Island. J. Geophys. Res., 116, D19103, https://doi.org/10.1029/2010JD015581.

- Splitt, M. E., and S. M. Lazarus, 2017: Gigantic jet environments: A meteorological evaluation using reanalysis data sets. 2017 Fall Meeting, New Orleans, LA, Amer. Geophys. Union, Abstract AE23A-2474.
- Su, H. T., and Coauthors, 2003: Gigantic jets between a thunder-cloud and the ionosphere. *Nature*, **423**, 974–976, https://doi.org/10.1038/nature01759.
- Sueki, K., and H. Niino, 2016: Toward better assessment of tornado potential in typhoons: Significance of considering entrainment effects for CAPE. *Geophys. Res. Lett.*, 43, 12597–12604, https://doi.org/10.1002/2016GL070349.
- Tsuda, T., 2014: Characteristics of atmospheric gravity waves observed using the MU (middle and upper atmosphere) radar and GPS (global positioning system) radio occultation. *Proc. Japan Acad.*, **90B**, 12–27, https://doi.org/10.2183/pjab.90.12.
- van der Velde, O. A., W. A. Lyons, T. E. Nelson, S. A. Cummer, J. Li, and J. Bunnell, 2007: Analysis of the first gigantic jet recorded over continental North America. *J. Geophys. Res.*, **112**, D20104, https://doi.org/10.1029/2007JD008575.
- Wang, P. K., 2003: Moisture plumes above thunderstorm anvils and their contributions to cross-tropopause transport of water vapor in midlatitudes. J. Geophys. Res., 108, 4194, https:// doi.org/10.1029/2002JD002581.
- —, 2004: A cloud model interpretation of jumping cirrus above storm top. *Geophys. Res. Lett.*, 31, L18106, https://doi.org/ 10.1029/2004GL020787.
- ——, 2007: The thermodynamic structure atop a penetrating convective thunderstorm. *Atmos. Res.*, **83**, 254–262, https:// doi.org/10.1016/j.atmosres.2005.08.010.
- —, S.-H. Su, M. Setvak, H. Lin, and R. M. Rabin, 2010: Ship wave signature at the cloud top of deep convective storms. *Atmos. Res.*, 97, 294–302, https://doi.org/10.1016/j.atmosres.2010.03.015.
- Whiteway, J. A., E. G. Pavelin, R. Busen, J. Hacker, and S. Vosper, 2003: Airborne measurements of gravity wave breaking at the tropopause. *Geophys. Res. Lett.*, **30**, 2070, https://doi.org/10.1029/2003GL018207.
- Witt, A., D. W. Burgess, A. Seimon, J. T. Allen, J. C. Snyder, and H. B. Bluestein, 2018: Rapid-scan radar observations of an Oklahoma tornadic hailstorm producing giant hail. Wea. Forecasting, 33, 1263–1282, https://doi.org/10.1175/WAF-D-18-0003.1.
- WMO, 1957: Meteorology—A three-dimensional science. WMO Bull., 6, 134–138.
- Zelinsky, D. A., 2019: Tropical Depression Three (AL032019): 22–23 July. National Hurricane Center Tropical Cyclone Rep., 8 pp.

Copyright of Journal of the Atmospheric Sciences is the property of American Meteorological Society and its content may not be copied or emailed to multiple sites or posted to a listserv without the copyright holder's express written permission. However, users may print, download, or email articles for individual use.